Research Square

Preprints are preliminary reports that have not undergone peer review.
They should not be considered conclusive, used to inform clinical practice,
or referenced by the media as validated information.

Inhibition of CGRP receptor ameliorates AD pathology by reprogramming lipid metabolism through HDAC11/LXRβ/ABCA1 signaling

Fang Huang

huangf@shmu.edu.cn

Fudan University

Guangchun Fan

Fudan university

Fangzheng Chen

Fudan university

Min Liang

Fudan university

Ping Yang

Fudan university

Hongtian Dong

Fudan university

Jing Su

Fudan university

Mengqi Wang

Fudan university

Ziyuan Wang

Fudan university

Penggang Ning

Fudan university

Chenye Shen

Fudan university

Xiwen Tang

Fudan university

Xin Yan

Fudan university

Haoxiang Lin

Fudan university

Jiayin Zhao

Fudan university
Yunhe Zhang
Fudan university
Zhesu Cheng
Fudan university
Hui Lu
School of Basic Medical Sciences, Fudan University
Xiuping Liu
Fudan university
Renyuan Zhou
Fudan university
Yang Luan
Fudan university
Li Cao
Naval Medical University (Second Military Medical University, SMMU)
Mei Yu
Fudan university
Wensheng Li
Fudan University https://orcid.org/0000-0001-9276-6529
Jian Fei
Tongji University https://orcid.org/0000-0001-7755-0818
Ruling Shen
Fudan university

Article

Keywords:

Posted Date: April 21st, 2026

DOI: https://doi.org/10.21203/rs.3.rs-9358637/v1

License: This work is licensed under a Creative Commons Attribution 4.0 International License.
Read Full License

Additional Declarations: There is **NO** Competing Interest.

Abstract

The Calcitonin gene-related peptide (CGRP) receptor has gained attention in Alzheimer's Disease (AD) research due to its involvement in regulating neuroinflammation, but its role and mechanism in AD pathology remain unclear. Here, we demonstrate that CALCRL, a core component of the CGRP receptor, is upregulated in the hippocampus of AD dementia patients and 5×FAD mice. Knockout of the CGRP receptor ligand Calca or pharmacological blockade using Rimegepant (Rim), attenuates soluble Aβ1-42 oligomer-induced neuronal death and glial inflammation, and ameliorates neurobehavioral deficits and AD pathology in 5×FAD mice. Mechanistically, these effects are mediated through HDAC11 inhibition, which enhances LXRβ acetylation and ABCA1 expression, reprogramming the lipid metabolism of neurons and glia. Importantly, the CALCRL/HDAC11/LXRβ/ABCA1 axis is conserved across both humans and mice. Our data uncover a novel mechanism underlying AD pathogenesis and highlight the therapeutic potential of targeting CGRP signaling in AD.

Main

Alzheimer's disease (AD) is the leading cause of dementia worldwide, characterized by multiple pathological features in the brain, including amyloid-β (Aβ) plaques, tau tangles, neuroinflammation, and synaptic terminal damage[1,2]. However, strategies to slow or prevent its clinical progression remain elusive, identifying new and effective therapeutic targets is critical.

The Calcitonin Gene-Related Peptide (CGRP) receptor is a complex composed of multiple proteins, with two critical transmembrane proteins-calcitonin receptor-like receptor (CALCRL) and receptor activity-modifying protein 1 (RAMP1)-playing key roles in mediating the effects of CGRP [3-7]. CGRP is a 37-amino acid neuropeptide that exists in two forms, α and β CGRP, with the α CGRP predominantly transcribed from the calcitonin-CGRP gene (CALCA) and playing a major role in the central nervous system (CNS) [8]. CGRP and its receptors are present in several regions of the CNS, including the dorsal horn of the spinal cord, the trigeminal nucleus caudalis, the dorsal and trigeminal ganglia, the periaqueductal gray, the amygdala, and the thalamus [9,10]. The distribution of CGRP and its receptor in these regions highlights their pivotal involvement in pain modulation, neuroinflammatory processes, and neurovascular regulation, particularly in conditions such as migraine and other neurovascular disorders [11-13]. Emerging research underscores neuroinflammation as a crucial mechanism in migraine, indicated by glial activation and elevation of inflammatory mediators such as IL-1β, TNF-α, IL-6 and NLRP3 [14-17]. Neuroinflammation also represents a key pathological driver in both the initiation and progression of AD [18,19], however, the specific role and underlying mechanism of the CGRP receptor signaling in AD remain to be elucidated.

In the present study, we demonstrate that CALCRL is upregulated in both AD patients and 5×FAD mice. Pharmacological inhibition of CGRP signaling using Rimegepant (Rim) or genetic deletion of its ligand (Calca) protects against Aβ-induced neuronal damage and glial inflammation *in vitro. In vivo*, deletion of *Calca* or inhibition of CGRP receptor also improves cognition and reduces amyloid burden, tau pathology,

and glial activation in 5×FAD mice, especially in the hippocampus. Multi-omics analyses identified HDAC11 downregulation as a key mechanism underlying these effects. Finally, it was revealed that the protective effect of HDAC11 inhibition in AD depends on the maintenance of LXRβ acetylation, which enhances ABCA1 expression, reprogramming the lipid metabolism of neurons and glia. This molecular cascade is further supported by the observation that HDAC11 is strongly upregulated in AD dementia patients and 5×FAD mice, and its expression is negatively correlated with ABCA1 levels. These findings uncovered a novel role of CGRP receptor in regulating lipid metabolism and neuroinflammation via the HDAC11/LXRβ/ABCA1 axis, highlighting a potential therapeutic strategy for AD.

CALCRL is upregulated in patients with Alzheimer's dementia and 5×FAD mice

To investigate the expression pattern of CALCRL in AD, we queried the Seattle Alzheimer's Disease Brain Cell Atlas (SEA-AD) database, which includes single-nucleus RNA sequencing (snRNA-Seq) data from the middle temporal gyrus (MTG) of 33 male and 51 female donors (Fig.1a) [20,21]. The results showed that CALCRL tends to be more highly expressed in multiple cell types in both the older dementia and no-dementia groups, compared with reference genomes from younger individuals (Fig.1b,c). Additionally, we retrieved occipital cortex snRNA-Seq data from the NCBI database (https://www.ncbi.nlm.nih.gov/) using the accession code GSE148822, which includes data from 3 male and 7 female AD donors (Extended Data Fig.1a) [22]. Consistent with the SEA-AD database results, this dataset also showed a tendency for higher CALCRL expression in old dementia and no-dementia individuals compared with younger controls (Extended Data Fig.b-f). To further evaluate CALCRL protein expression, we conducted Western blotting and immunohistochemical analyses on hippocampal samples from both male (n=3) and female (n=3) dementia and non-dementia participants (Fig.1d and Extended Data Fig.1g), and found that CALCRL protein level was significantly increased in dementia patients compared with no-dementia controls (Fig.1e,f). Similarly, we examined CALCRL expression in the hippocampus of 5×FAD mice and obtained consistent findings: CALCRL was upregulated in both female and male 5×FAD mice (Extended Data Fig.1h). These results suggest that the expression and function of CALCRL may play a crucial part in the pathological processes of AD.

Inhibition of CGRP receptor reduces primary neuronal cell death and glial inflammation induced by soluble Aβ1-42 oligomers

Initially, we conducted molecular docking simulations of Rim, a well-recognized CGRP-receptor antagonist, on the crystal structure of the ectodomain complex of the CGRP receptor (PDB: 3N7R). It revealed that Rim establishes two hydrogen bonds with THR122 and ARG119, respectively (Extended Data Fig.1i). Accumulating evidence indicates that soluble Aβ1-42 oligomers (sAβ1-42) are closely linked to the pathogenesis of AD. To investigate whether the CGRP receptor modulates neuronal and glial responses to sAβ1-42-induced injury, we prepared sAβ1-42 from synthetic mouse Aβ1-42 monomers, as described [23]. Scanning electron microscopy (SEM) images of purified fibrin clots revealed the formation of aggregates in the presence of Aβ1-42, suggesting that sAβ1-42 was successfully prepared (Extended Data Fig.1j). Subsequently, we isolated and cultured primary mixed glial cells and

cortical and hippocampal neurons from both WT and *Calca*$^{-/-}$ mice, treated with 10 μM sAβ1-42, with or without Rim, for 24 hours *in vitro* (Extended Data Fig.1j). *Calca* deficiency only exhibited no significantly influence on the viability of primary neurons (Extended Data Fig.1k,l). In contrast, treatment with Rim at concentrations of 0.1 and 1 μM or *Calca* knockout following sAβ1-42 exposure, significantly enhanced neuronal viability compared with the control group (Extended Data Fig.1l). This protective effect was further corroborated by Hoechst 33342/propidium iodide (PI) staining (Extended Data Fig.1m). Furthermore, the mRNA levels of proinflammatory factors were measured in primary mixed glial cells treated with sAβ1-42 for 24 hours, with or without 1 μM Rim. Notably, a significant reduction in *Il-1β* and *NOS2* expression was detected in the Rim + sAβ1-42 group compared with the sAβ1-42 group. Additionally, in the *Calca*$^{-/-}$ + sAβ1-42 group, the expression levels of *Il-1β*, *NOS2*, and *Il-6* were significantly downregulated compared with the WT + sAβ1-42 group (Extended Data Fig.1n). Collectively, these findings highlight the potential of CGRP receptor inhibition as a promising therapeutic approach for the treatment of AD.

Calca deficiency ameliorates cognitive decline in 7-month-old 5×FAD mice

Given the protective effects of CGRP receptor inhibition against sAβ1-42 induced neurotoxicity in vitro, we hypothesized that genetic deletion of its ligand *Calca* may ameliorate cognitive decline in the AD mouse model. To investigate the impact of *Calca* deficiency on cognitive alterations in mice, we crossbred two types of transgenic mice, namely the 5×FAD and *Calca* deficient mice (Fig.1g,h). Subsequently, we evaluated the anxiety/depression behaviors and cognitive functions of the resulting offspring (5×FAD and 5×FAD;Calca$^{-/-}$mice) (Fig.1i,l). Our findings showed that *Calca* deficiency significantly increased the frequency of entries into the central area in the Open field test (OF) in female 5×FAD mice (Fig.1k,l) and significantly reduced the anxiety index in the elevated plus maze (EPM) (Fig.1m,n). In contrast, *Calca* deficiency had no effect on immobility time in the Forced swimming test (FST). To further assess the impact of *Calca* deficiency on memory, we performed novel object recognition (NOR) and novel location recognition (NLR) tests. *Calca* deficiency significantly enhanced novel object recognition in female 5×FAD mice, but did not affect novel location recognition (Fig.1p-r). In the Y-maze test, *Calca* deficiency significantly increased spontaneous alternation compared to 5×FAD controls (Fig.1s,t). Hippocampus-dependent spatial memory was further evaluated using the Morris water maze (MWM). During training, *Calca* deficiency significantly reduced the latency to locate the platform on day 6 in male 5×FAD mice and on day 5 in females (Fig.1u,v). In the probe test, female 5×FAD;Calca$^{-/-}$ mice showed more platform crossings and spent less time in non-target quadrants (Fig.1w-y), whereas males spent more time in the target quadrant and exhibited a trend toward increased platform crossings (p = 0.0573). Together, these results suggest that *Calca* deficiency ameliorates anxiety/depression behaviors and memory deficits in AD mice.

Calca deletion reduces Aβ burden and glial activation in 7-month-old 5×FAD mice

To explore the mechanisms underlying the beneficial effects of *Calca* deficiency on cognitive functions, we examined key pathological features of AD. Thioflavin-S staining revealed a significant reduction in Aβ

plaque number in the hippocampus (HP) of male 5×FAD;Calca$^{-/-}$ mice, whereas no significant change was observed in the cortex (CTX) (Fig. 2a-e). In contrast, female 5×FAD;Calca$^{-/-}$ mice exhibited a significant decrease in Aβ plaque number in both the HP and CTX compared with 5×FAD controls (Fig.2a-e). In addition, *Calca* deletion significantly decreased plaque size in the AD mouse model (Fig.2a-e). Elisa analyses further showed that both soluble and insoluble Aβ42 levels were significantly reduced in 5×FAD;Calca$^{-/-}$ mice, whereas Aβ40 remained unchanged (Fig.2f-i). The above findings were further supported by the effects of *Calca* delation on amyloid precursor protein (APP) levels. 5×FAD;Calca$^{-/-}$ mice exhibited significantly reduced APP levels in the hippocampus, whereas in the cortex, this reduction was observed only in females (Fig.2j,k,m,n). Hyperphosphorylated tau (P-tau) is another critical pathological feature of AD, as tau hyperphosphorylation triggers pathological changes, including synaptic impairment [24]. To assess the impact of *Calca* deficiency on tau pathology, we measured P-tau (S396) levels and found a significant reduction in female 5×FAD;Calca$^{-/-}$ mice (Fig.2j,l,m,o). Collectively, these findings indicate that loss of *Calca* markedly attenuates Aβ aggregation and inhibits the hyperphosphorylation of tau proteins in the mouse model of AD.

The proliferation and activation of microglia, particularly those surrounding amyloid plaques, are remarkable characteristics of AD [25]. Activated microglia can aggravate tau pathology and release inflammatory factors that harm neurons directly or indirectly via astrocyte-mediated neurotoxicity [26]. To evaluate the effect of *Calca* deficiency on neuroinflammation, we assessed astrocytosis and microgliosis via Western blot and glial fibrillary acidic protein (GFAP) and ionized calcium-binding adaptor molecule 1 (IBA1) staining. As shown in Fig.2j,k,m,n, *Calca* deficiency reduced GFAP expression in the hippocampus of both sexes and in the cortex of female mice, whereas IBA1 levels were decreased only in the hippocampus of female mice. Confocal microscopy of the HP and CTX revealed that Calca deficiency reduced the number of GFAP$^+$ astrocytes in both regions of female mice, whereas IBA1$^+$ microglia were decreased only in the HP of females (Fig.2p-r). Furthermore, *Calca* deletion reduced the number of microglia and astrocytes surrounding Aβ plaques in 5×FAD mice (Fig.2p-r). Fluorescent immunohistochemistry was performed to quantify CD68$^+$/IBA1$^+$ and C3$^+$/GFAP$^+$ areas in the HP and CTX (Fig.2s-u). Within microglia, the CD68$^+$ area was reduced in 5×FAD;Calca$^{-/-}$ mice compared to 5×FAD controls (Fig.2s-u), whereas the C3$^+$ area in astrocytes was decreased only in females (Fig.2v-x). All imply that *Calca* deficiency attenuates astrocytosis and microgliosis, and reduces the abundance of disease-associated microglia (DAM) and astrocytes (DAA) in 5×FAD mice.

CGRP receptor antagonist Rim improves behavioral performance in AD worms and 7-month-old 5×FAD mice

To further investigate the therapeutic potential of Rim in mitigating Aβ-induced pathology, we utilized both the transgenic *Caenorhabditis elegans* AD model (Punc-54::Aβ1–42, strain CL2006), which exhibits progressive adult-onset paralysis (Extended Data Fig.1o), and the 5×FAD mouse model. As shown in Extended Data Fig.1p, treatment with 2 μM Rim significantly delayed the onset of Aβ-induced paralysis in CL2006 nematodes. Since Rim orally disintegrating tablets (75 mg) are typically administered daily for

acute migraine treatment and every other day for migraine prevention [27], we adopted a regimen of alternate-day intraperitoneal injections of Rim (10mg/kg) in 7-month-old 5×FAD mice for a duration of one month (Fig.3a).

We then evaluate the effects of Rim on anxiety- and depression-like behaviors in 5×FAD mice (Fig.3b). Our findings revealed that Rim treatment significantly increased both the frequency and duration of entries into the central area in the OF (Fig.3c,d), indicating reduced anxiety-like behavior. Additionally, Rim significantly lowered the anxiety index in the EPM, particularly in female 5×FAD mice (Fig.3e). Furthermore, in male 5×FAD mice, Rim treatment markedly reduced immobility time in the FST (Fig.3f), suggesting an antidepressant-like effect.

The effects of Rim at the selected doses on learning and memory were further evaluated. The Y-maze test revealed that Rim treatment significantly and substantially reversed the alternation deficits only observed in female 5×FAD mice (Fig.3g,h). To further assess the impact of Rim on memory, we employed the NLR and NOR tests. Male 5×FAD mice exhibited deficits in NLR, while female 5×FAD mice displayed impairments in NOR (Fig.3j,k). Notably, Rim treatment significantly restored the ability of male mice to recognize novel locations and female mice to recognize novel objects (Fig.3j,k). Finally, the MWM test was used to examine hippocampus-dependent spatial memory. During the training phase, Rim-treated male 5×FAD mice demonstrated a significantly reduced latency to find the platform on day 5 (Fig.3k,l). In the test phase, Rim-treated male mice also exhibited more platform crossings and less time spent outside the platform quadrant (Fig.3m,n). In contrast, Rim-treated female 5×FAD mice displayed a significant increase in the time spent in the platform quadrant during the test phase, but no difference observed in other measures (Fig.3m,n). These findings suggest that Rim exerts sex-dependent effects on learning and memory, with notable improvements in specific cognitive domains across both male and female 5×FAD mice.

CGRP receptor antagonist Rim alleviates AD-related pathology

To investigate whether key AD pathological features were affected by Rim. The number and size of Aβ plaques were also quantified in the cortex and hippocampus respectively. As expected, 5×FAD mice exhibited a significant increase in Aβ plaques (Fig.3o-q and Extended Data Fig.2a-c). Notably, Rim administration led to a sex-specific reduction in Aβ pathology. In female 5×FAD mice, Rim treatment resulted in more than a 50% decrease in plaque number and total plaque area in the hippocampus, along with a significant reduction in total plaque area in the cortex (Fig.3o-q and Extended Data Fig.2a-c). In male 5×FAD mice, Rim significantly reduced the total plaque area in the hippocampus, though the effect was less pronounced compared with females (Fig.3o-q and Extended Data Fig.2a-c). Both soluble and insoluble Aβ40/Aβ42 were increased in 5×FAD mice, whereas Rim administration led to significant reductions in female mice. Although male mice showed a similar trend for insoluble Aβ42 reduction (p=0.0629) (Extended Data Fig.2d-g). Overall, these results suggest that Rim mitigates Aβ pathology in a sex-dependent manner, with more robust effects observed in female 5×FAD mice.

Rim-treated 5×FAD mice exhibited significantly reduced APP levels in the hippocampus, while only a decreasing trend was observed in the cortex (p = 0.0781) (Fig.3t,u and Extended Data Fig.2j,k). By analyzing the expression level of P-tau (S396), we observed a significant reduction in P-tau levels in the hippocampus of Rim-treated 5×FAD mice (Fig.3t,v, Extended Data Fig.2j,l). Our results verify that Rim alleviates Aβ accumulation and inhibits the hyperphosphorylation of tau proteins, particularly in the hippocampus.

To evaluate Rim's effect on neuroinflammation, we assessed astrocytosis and microgliosis via GFAP and IBA1 staining and Western blot. As depicted in Fig.3r,s and Extended Data Fig.2h,i, all revealed an increase of microglia and astrocytes in the hippocampus and cortex of 5×FAD mice, with a noted decrease in astrocytes following Rim administration. Furthermore, Rim reduced the number of microglia and astrocytes surrounding Aβ plaques in 5×FAD mice. Meanwhile, Rim significantly downregulated GFAP and IBA1 protein levels in both regions of female 5×FAD mice (Fig.3t,u and Extended Data Fig.2j,k). However, in male 5×FAD mice, Rim only led to a decrease in GFAP expression in the hippocampus, with IBA1 showing a downward trend without reaching statistical significance (Fig.3t,u and Extended Data Fig.2j,k). On a per-cell basis, there was a significant decrease in $CD68^+/IBA1^+$ and $C3^+/GFAP^+$ areas (Fig.3w-z and Extended Data Fig.2m-p). Furthermore, through IBA1 immunohistochemistry and morphological analysis, microglia surrounding plaques in 5×FAD mice exhibited an amoeboid shape with somatic hypertrophy, whereas Rim-treated microglia generally displayed reduced cell bodies (Extended Data Fig.2q-t). Additionally, we evaluated the RNA expression levels of inflammation-related cytokines. In 5×FAD mice, Rim significantly reduced *Il-1β* levels in the hippocampus at both genders but increased *Tgf-β* levels only in female mice, while *Il-6* level significantly decreased in male mice (Extended Data Fig.2u). In the cortex, Rim significantly reduced *Il-6* expression and increased *Tgf-β* level in female 5×FAD mice (Extended Data Fig.2v). Altogether, these findings indicate that Rim mitigates neuroinflammation and modifies the microglial and astrocytic proliferation in 5×FAD mice.

CGRP receptor antagonist Rim reverses alterations in the immune-inflammatory pathways and lipid metabolism in AD mice via Multi-omics analysis

To delve deeper into the mechanisms underlying the impact of Rim on AD pathology, we conducted a comprehensive multi-omics analysis. Initially, RNA sequencing (RNA-seq) analysis was carried out on hippocampal tissues from 5×FAD mice, as depicted in Extended Data Fig.3a. We identified a set of differentially expressed genes (DEGs): 955 DEGs between 5×FAD+Veh(F) and WT+Veh(F) (Extended Data Fig.3b), 717 DEGs between 5×FAD+Veh(M) and WT+Veh(M) (Extended Data Fig.3c), 1053 DEGs between 5×FAD+Rim(F) and WT+Veh(F) (Extended Data Fig.3d), and 591 DEGs between 5×FAD+Rim(M) and WT+Veh(M) (Extended Data Fig.3e). Functional annotation of the DEGs, considering both Rim treatment and AD condition, was performed using Gene Ontology (GO) analysis. It was revealed that the most significantly impacted biological processes were related to immune responses (Extended Data Fig.3f-i). Gene Set Enrichment Analysis (GSEA) was employed to identify subtle yet significant expression changes across gene sets linked by common pathway functions, which might not be discernible through direct gene comparison. Through GSEA, we examined inflammatory pathways as cataloged in the Kyoto

Encyclopedia of Genes and Genomes (KEGG). As shown in Extended Data Fig.3j, the analysis highlighted significant enrichment of several KEGG inflammatory pathways across the four groups, including the TNF signaling pathway, MyD88-dependent toll-like receptor signaling pathway, JAK-STAT signaling pathway, regulation of lipopolysaccharide-mediated signaling pathway, and inflammatory bowel disease. Notably, in the comparison between the Rim-treated groups and their vehicle (Veh) counterparts, the Veh-treated group showed greater enrichment in the Cytokine-cytokine receptor interaction pathway, NF-κB pathway, JAK-STAT signaling pathway, lipopolysaccharide-mediated signaling pathway, and Toll-like receptor signaling pathway.

Subsequently, we performed proteomic analysis using mass spectrometry (MS) to evaluate the impact of Rim on protein expression levels in the hippocampal tissues of 5×FAD mice (Extended Data Fig.3k). Approximately 100 differentially expressed proteins (DEPs) were identified in each group when compared with their respective control groups (Extended Data Fig.3l). Consistent with the transcriptomic findings, the top five KEGG-enriched pathways for DEPs in these groups were predominantly associated with immune-inflammatory processes. These pathways included complement and coagulation cascades as well as staphylococcus aureus infection, identified in the 5×FAD+Veh(F) vs. WT+Veh(F), 5×FAD+Veh(M) vs. WT+Veh(M), and 5×FAD+Rim(F) vs. WT+Veh(F) comparisons. Additionally, the JAK-STAT signaling pathway was enriched in the 5×FAD+Veh(F) vs. WT+Veh(F) group, while Yersinia infection and the chemokine signaling pathway were enriched in the 5×FAD+Veh(M) vs. WT+Veh(M) group (Extended Data Fig.3m,n). Taken together, these findings suggest that Rim may exert its neuroprotective effects by modulating several immune-inflammatory pathways at both the transcriptional and translational levels.

We next performed weighted gene co-expression network analysis (WGCNA) on all 56,691 genes across 18 samples to further investigate the mechanisms underlying the beneficial effects of Rim in 5×FAD mice. The sample dendrogram and trait heatmap are presented in Extended Data Fig.4a. Hierarchical clustering identified 27 distinct modules (Extended Data Fig.4b), with the branches of the dendrogram (meta-modules) grouped based on eigengene correlations (Extended Data Fig.4c). Among these, three modules-tan, dark grey, and brown-exhibited a robust and statistically significant positive correlation with the 5×FAD group, while being negatively correlated with the WT and Rim-treated groups (Extended Data Fig.4d and Fig.4a). To refine our analysis, we conducted Mfuzz clustering based on gene expression patterns to identify genes with high expression in Veh-treated 5×FAD mice. This analysis yielded 20 gene expression clusters, of which only Cluster 5 met our criteria: genes highly expressed in the Veh-treated 5×FAD group but attenuated in the Rim-treated 5×FAD group (Extended Data Fig.4e). To identify hub genes associated with Rim's effects in AD, we performed an intersection analysis between the three WGCNA modules and Cluster 5, resulting in 683 intersecting genes, which we termed RNA-seq-Rim Pharmaco-genes (RNA-seq-RPGs) (Fig.4b). Similarly, we applied the Mfuzz algorithm to soft-cluster proteins and identified two clusters, Cluster 3 and Cluster 20, which we designated as MS-Rim Pharmaco-proteins (MS-RPPs) for further investigation (Extended Data Fig.4f).

Immune-inflammatory and metabolic pathways engage in reciprocal regulation [28-30]. To further investigate the impact of Rim on the metabolism of 7-month-old 5×FAD mice, we performed KEGG metabolic pathway enrichment analysis using RNA-seq-RPGs and MS-RPPs. Pathways associated with sugar and lipid metabolism were significantly enriched at both the RNA and protein levels. These included glycerophospholipid metabolism, carbon metabolism, and nucleotide sugar biosynthesis at the transcriptomic level, as well as N-glycan biosynthesis, fatty acid metabolism, and glycerophospholipid metabolism at the proteomic level (Extended Data Fig.4c,d).

To distinguish the activity levels of lipid and carbohydrate metabolism in 5×FAD mice, we analyzed the expression patterns of genes involved in these pathways across different experimental groups. The results revealed that lipid metabolism was more active, as genes related to this pathway showed greater dispersion in the ternary plot compared with those involved in carbohydrate metabolism, in both female and male 5×FAD mice (Extended Data Fig.5a,b).

To identify specific lipid species dysregulated in 5×FAD mice, we conducted lipidomic profiling of hippocampal tissues (Fig.4e). PCA analysis revealed that the principal components of 5×FAD-Veh mice were significantly separated from the Veh-WT group, whereas 5×FAD-Rim mice were not significantly separated from Veh-WT mice (Fig.4f). Among the 700+ lipid species measured in the hippocampus, we identified 28 differentially expressed lipids (DELs) in 5×FAD+Veh(F) vs. WT+Veh(F) (Fig.4g), 50 DELs in 5×FAD+Veh(M) vs. WT+Veh(M) (Fig.4h), 18 DELs in 5×FAD+Rim(F) vs. WT+Veh(F) (Fig.4i), and 36 DELs in 5×FAD+Rim(M) vs. WT+Veh(M) (Fig.4j). Notably, among the decreased lipids were triacylglycerol (TAG) and diacylglycerol (DAG) species, while cholesteryl ester (CE) and lysophosphatidylcholine (LPC) species were significantly increased (Fig.4g-j). These findings highlight specific disruptions in cholesterol and fatty acid metabolism in 7-month-old 5×FAD mice. Emerging research in AD has increasingly focused on identifying lipid signatures associated with neuroinflammation and pathologies, including alterations in monoacylglycerol (MAG), LPC, CE, and ceramide (CER) species [31,32]. When comparing the cumulative effects on hippocampal lipidomes between WT, Veh-5×FAD, and Rim-5×FAD mice, we observed significant elevations in LPC, CE, and CER levels in Veh-5×FAD mice (Fig.4k). Remarkably, treatment with Rim substantially mitigated these alterations (Figu.4k). To further investigate the effect of Rim on lipid accumulation, we performed BODIPY staining in the hippocampus and observed a significant reduction in BODIPY signals especially in microglia of Rim-treated 5×FAD mice (Fig.4l,m). These results suggest that Rim may synergistically rescue impaired cholesterol metabolism, improve endolysosomal lipid clearance, and reduce neuroinflammation in 7-month-old 5×FAD mice.

HDAC11 downregulation is key to the protective effects of CGRP receptor antagonist Rim in the hippocampus of AD mice

To identify the molecular mediators underlying Rim' effects on AD pathology, we intersected the RNA-seq-RPGs with the MS-RPPs, identifying 26 genes that were strongly correlated with Rim’s efficacy at both the transcriptional and translational levels (Fig.4n). A combined heatmap of gene and protein expression showed that all 26 genes followed a consistent trend: they were highly upregulated in Veh-

treated 5×FAD mice and attenuated in Rim-treated 5×FAD mice (Fig.4o). Interestingly, nearly half of these genes are known to regulate inflammation (e.g., *Borcs5*, *Hdac11*, *Slc35a2*, *Chtop*, *Hnrnpa2b1*, *Emc3*, *Kcmf1*, *Dgka*, *Dnaja3*, *Smarcb1*, *Wdsub1*), while five others (*Nop56*, *Srsf6*, *Hnmpa1*, *Golm1*, *Srsf2*) have been implicated in AD progression (Fig.4p). Notably, *Hdac11* emerged as a particularly intriguing target. As the sole member of the class IV HDAC subfamily [33], HDAC11 has received little attention in the context of AD, despite reports linking other HDAC family members (HDAC3, HDAC5, HDAC6) to the disease (Fig.4p) [34-36]. Based on these findings, we speculate that HDAC11 may play a critical role in mediating the neuroprotective and anti-inflammatory effects of Rim in 5×FAD mice.

We further examined the changes of *Hdac11* expression in the brains of 5×FAD mice and observed a significant upregulation of both transcription and protein levels in the hippocampus of 5×FAD mice, except for *Hdac11* transcript levels in male 5×FAD mice (Fig.4q-s). Rim significantly reversed the protein levels of HDAC11 in the hippocampus of 5×FAD mice at both genders (Fig.4q,r). However, the mRNA expression of *Hdac11* was only significantly reversed in female 5×FAD mice, suggesting a sex-specific effect and highlighting the close association between *Hdac11* and the efficacy of Rim in the hippocampus of 5×FAD mice (Fig.4s). Consistent with these changes, immunofluorescence confirmed that Hdac11 is mainly expressed in neurons (>80% $NeuN^+$) with little colocalization with GFAP (Fig.4t).

Given that HDAC11 has been reported to promote the NLRP3/caspase-1/GSDMD pathway, leading to pyroptosis via the regulation of ERG acetylation in human umbilical vein endothelial cells [37], we hypothesize that the neuroprotective effects of Rim in the hippocampus of 5×FAD mice may involve the HDAC11-NLRP3 inflammasome pathway. To validate this hypothesis, we performed qPCR and found that the expression of *Nlrp3* was significantly upregulated in the hippocampus of 5×FAD mice, while Rim significantly downregulated *Nlrp3* mRNA levels in female 5×FAD mice, but not in males (Fig.4u). To further explore the relationship between *Hdac11* and *Nlrp3*, we performed a correlation analysis of their mRNA expression levels in the hippocampus of 5×FAD mice. The results revealed a significant positive correlation between *Hdac11* and *Nlrp3* expression at both genders (Fig.4v,w). Taken together, our data suggest that HDAC11 may serve as a critical mediator of Rim's neuroprotective effects in the hippocampus of 5×FAD mice.

HDAC11 inhibition mitigates neuronal cell death induced by sAβ1-42 *in vitro* and alleviates paralysis in *Caenorhabditis elegans* CL2006.

To further investigate the cell-specific expression of HDAC11 in AD, we retrieved snRNA-Seq data from the SEA-AD database [20]. As shown in Extended Data Fig.6a-d, HDAC11 is widely expressed across various brain cell types, including neurons, microglia, and astrocytes. We then evaluated the effects of CGRP receptor antagonist Rim on HDAC11 level in primary neurons and mixglia treated with 1 μM Rim with or without 10 μM sAβ1-42 for 24 h (Extended Data Fig.6e). Our analysis revealed a significant increase in HDAC11 expression in both primary neurons and mixed glial cells following treatment with sAβ1-42 (Extended Data Fig.6f-h). Although 24 h of Rim treatment did not markedly decrease HDAC11 expression in mixglia, we observed a significant reduction of HDAC11 levels in primary neurons treated

with Rim (Extended Data Fig.6f-h). These findings suggest that Rim may exert exerts its neuroprotective effects predominantly by directly modulating HDAC11 activity in neurons. To further explore the role of HDAC11 in AD pathology, we examined the effects of the HDAC11 inhibitor Elevenostate (Ele) on neuronal responses to sAβ1-42-induced injury. Primary cortical neurons from WT mice were treated with 10 μM sAβ1-42 in the presence or absence of Ele for 24 h (Extended Data Fig.6i). The results of CCK8 assay and Hoechst 33342/PI staining indicated that Ele (10 μM) significantly improved cell viability compared with the sAβ1-42-treated group (Extended Data Fig.6j-l). Additionally, Ele at concentrations of 4 μM and 20 μM was found to alleviate paralysis in the Aβ1-42 transgenic *Caenorhabditis elegans* (CL2006) model of AD (Extended Data Fig.6n).

Short-term inhibition of hippocampal HDAC11 function reduced astroglial activation in 7-month-old female 5×FAD mice

To determine whether HDAC11 inhibition contributes to the protective effects of Rim on AD pathology and neuroinflammation *in vivo*, we performed bilateral stereotaxic injections of Ele into the CA1 region of the hippocampus in 5×FAD mice, followed by analysis one day post-injection (Extended Data Fig.7a). Thioflavin-S staining revealed no significant differences in Aβ plaque burden in the hippocampus of Ele-treated 5×FAD mice (Extended Data Fig.7b-d). Whereas, among other AD pathological markers, Ele treatment significantly reduced both the number of astrocytes and the expression level of GFAP proteins in the hippocampus of female 5×FAD mice (Extended Data Fig.7e-g). However, Ele did not have a significant impact on tau pathology, the number of microglia, or the expression levels of HDAC11, APP, and IBA1 (Extended Data Fig.7h-j). These findings suggest that Ele may confer a protective effect on the hippocampus of female 5×FAD mice, potentially through mechanisms involving astrocytic modulation.

***Hdac11* knockdown in the hippocampus of 7-month-old 5×FAD mice results in enhanced memory**

We further employed recombinant adeno-associated viral vectors (rAAV) to achieve a long-term neuron-specific RNAi-mediated *Hdac11* knockdown in the hippocampus of 5×FAD mice. rAAV vectors containing either hSYN-EGFP-shRNA-Hdac11 (shRNA-Hdac11) or hSYN-EGFP (shRNA-Control) were bilaterally injected into the hippocampal CA1 regions of 7-month-old 5×FAD mice (Fig.5a). One-month after viral injection, EGFP expression was observed broadly in the hippocampal pyramidal fields (including CA1, CA2, CA3, DG) of both groups (Fig.5b). Immunofluorescence analysis revealed that most EGFP-positive cells were co-labeled with NeuN but not with IBA1 or GFAP, confirming that the virus predominantly infected neurons (Fig.5c,d). Furthermore, protein analysis validated that HDAC11 expression was significantly reduced in the hippocampus of rAAV shRNA-Hdac11-injected mice compared with the control mice (Fig.5e). Anxiety-related behavioral assessments were conducted using the EPM and FST paradigms. We observed that *Hdac11* knockdown significantly reduced the anxiety index in female 5×FAD mice, as assessed by the EPM, but no significant changes were noted in the FST (Fig.5f,g). Memory related behavioral assessments were performed to evaluate the effect of *Hdac11* knockdown on the hippocampus-dependent spatial learning and memory. 5×FAD mice injected with rAAV shRNA-Hdac11 exhibited significant enhancements in the NLR test (Fig.5h), Y-maze test (Fig.5j), and MWM test

(Fig.5k-m). Specifically, shRNA-Hdac11-injected female mice recovered their ability in the NLR test (Fig.5h) and reversed alternation deficits in the Y-maze test (Fig.5j). Male AD mice also showed improved alternation performance in the Y-maze test (Fig.5j). In the MWM test, strikingly, female mice infected with rAAV shRNA-Hdac11 exhibited significantly shorter latencies to locate the platform on day 6 of training (Fig.5l). During the probe trial, 5×FAD mice injected with rAAV shRNA-Hdac11 demonstrated superior performance. Specifically, mice injected with rAAV shRNA-Hdac11 spent more time in the platform quadrant, and female mice also exhibited more platform crossings (Fig.5m). Collectively, these findings validate that *Hdac11* knockdown in the hippocampus of 5×FAD mice was sufficient to enhance hippocampus-dependent learning and memory.

AD-related pathology in the hippocampus of AD mice would be alleviated by knockdown of *Hdac11*

We further investigated AD-associated pathological changes in *Hdac11* knockdown 5×FAD mice. Thioflavin-S staining revealed a significant reduction in both the number and size of Aβ plaques in the hippocampus of 5×FAD mice injected with rAAV shRNA-Hdac11 (Fig.5n-p). Additionally, rAAV shRNA-Hdac11-infected mice exhibited a dramatic decrease in the astrocyte number and GFAP protein levels in the hippocampus (Fig.5q-s). Interestingly, while a reduction in microglial cell number was observed only in rAAV shRNA-Hdac11-treated female 5×FAD mice, both male and female AD mice with *Hdac11* knockdown showed a significantly reduced IBA1 protein expression (Fig.5t). Moreover, 5×FAD mice infected with rAAV shRNA-Hdac11 demonstrated a greater than 50% reduction in APP levels and a significant decrease in phosphorylated tau proteins in the hippocampus (Fig.5t). Furthermore, we performed BODIPY staining to assess lipid accumulation in the hippocampus of rAAV shRNA-Hdac11-injected mice and observed a significant reduction in BODIPY signal intensity in microglia (Fig.5u). Finally, to determine whether cholesterol dysregulated was rescued by *Hdac11* knockdown, we conducted lipidomic profiling of hippocampal tissues (Fig.5v). PCA analysis revealed that the principal components of shRNA-control treated mice were significantly separated from the shRNA-Hdac11 group in both gender (Fig.5w). We identified 28 upregulated lipids and 29 downregulated lipids in females (shRNA-Hdac11 *vs.* shRNA-control), and 34 upregulated lipids and 24 downregulated lipids in males (Fig.5x). Notably, most cholesterol-related metabolites were reduced following shRNA-mediated *Hdac11* knockdown (Fig.5y). In summary, the data emphasizes that *Hdac11* knockdown in hippocampal neurons is sufficient to alleviate the core pathological hallmarks and correct cholesterol-related lipid metabolic dysfunctions associated with AD.

Neuron-specific knockdown of *Hdac11* promotes the reprogramming of lipid metabolism and inflammatory pathways

We used scRNA-seq to examine the impact of neuronal *Hdac11* knockdown on lipid metabolism and inflammatory pathways across different cell types in 5×FAD mice. Single cells were sorted from the mouse hippocampus, and single-cell transcriptomes were generated using the 10x Genomics platform (Extended Data Fig.8a). After quality control, a total of 37860 single cells were plotted on uniform manifold approximation projection (UMAP) dimensions for visualization. Unsupervised clustering

revealed a total of 18 distinct clusters across all group (Extended Data Fig.8b), which were annotated based on differential expression of known cell-type-specific marker genes (Extended Data Fig.8c,d). The preponderance of cells captured by our scRNA-seq dataset were Oligodendrocyte, Microglia, Neurons, OPC, Astrocytes, Fibroblasts with significantly fewer T cells (Extended Data Fig.8e,f). scRNA-seq analysis revealed that Hdac11 was downregulated in the shRNA-Hdac11 group relative to control group, both in neurons (Extended Data Fig.8g-i) and globally (Extended Data Fig.8j). Furthermore, neuronal knockdown of *Hdac11* enhanced intercellular communication with astrocytes (Extended Data Fig.8k,l), whereas microglia exhibited reduced interaction with neurons (Extended Data Fig.8m,n). After identifying differentially expressed genes across various cell types (Extended Data Fig.8o,p), we analyzed suppressed biological process pathways in neurons, astrocytes, and microglia. This analysis revealed cell type– and sex–specific downregulation of inflammation-related pathways—for example, the positive regulation of receptor signaling via STAT in female astrocytes, regulation of immune response in female microglia, and response to abiotic stimulus in male microglia, among other inflammation-related pathways (Extended Data Fig.8q,r). To further identify changes in metabolic and inflammatory pathways in different cell types, we performed GSVA analysis. As shown in Extended Data Fig.8s, neuronal knockdown of *Hdac11* enhanced ABC transporter pathway activity across multiple cell types, including neurons. It also reprogrammed several metabolic pathways—such as fatty acid metabolism, glycerophospholipid metabolism, and linoleic acid metabolism—in a sex-dependent manner. Additionally, distinct changes were observed in inflammatory pathways, including the WNT signaling pathway and the cytokine–cytokine receptor interaction pathway. Notably, the WNT signaling pathway was downregulated to varying degrees in oligodendrocytes, microglia, and astrocytes compared with the control group (Extended Data Fig.8s).

Knockdown of *Hdac11* exerts a protective role in AD by targeting LXRβ/ABCA1 axis

To investigate the potential regulatory mechanisms of HDAC11, we isolated hippocampal lysis from WT mice and performed immunoprecipitation with HDAC11 antibody or IgG followed by mass spectrometry (IP-MS) analysis (Fig.6a). Correlation analysis of enriched proteins revealed a higher degree of similarity between samples within the same antibody group compared with samples from different antibody group (Fig.6b). After excluding proteins that interacted with IgG, which were defined as non-specific bindings, we identified a total of 154 highly specific HDAC11-interacting proteins (Fig.6c). Subsequent KEGG pathway annotation classified these 154 Hdac11-interacting proteins into pathways associated with neurodegenerative diseases, inflammation, and lipid metabolism (Fig.6d). In parallel, hippocampal lysates from WT and *Calca*$^{-/-}$ mice were immunoprecipitated using acetylated lysine antibody to identify highly acetylated proteins that may serve as potential HDAC11 targets. Correlation analysis again showed a higher degree of similarity between samples within the same genotype group compared with samples from different genotype group (Fig.6e). We also identified 74 highly acetylated proteins in the *Calca*$^{-/-}$ group (Fig.6f). To further refine the list of potential functional Hdac11 target proteins, we intersected the 74 highly acetylated proteins from the *Calca*$^{-/-}$ group with the 154 Hdac11-interacting proteins identified via IP-MS (Fig.6c). This analysis yielded 27 candidate proteins for further investigation

(Fig.6h). Among these candidates, the protein of primary interest is NR1H2 (also known as LXRβ), due to its critical role in promoting the expression of ABCA1. Enhanced Abca1 expression has been shown to improve cognitive function in multiple AD mouse models by regulating lipid metabolism and exerting potent anti-inflammatory effects through the suppression of pro-inflammatory gene expression [38,39]. Notably, an evolutionary conservation analysis of NR1H2/LXRβ across four species revealed that three lysine residues near the N-terminal and C-terminal regions are highly conserved, suggesting these lysine residues may perform an evolutionarily conserved function (Fig.6i). Therefore, NR1H2/LXRβ may represent a key target through which Hdac11 inhibition exerts its neuroprotective and anti-inflammatory effects in 5×FAD mice.

To further explore this interaction, we performed molecular docking of HDAC11 with NR1H2/LXRβ. This analysis identified 10 binding modes between HDAC11 and LXRβ, with confidence scores ranging from 0.8634 to 0.9569 and docking scores spanning from -242.19 to 304.95 (Extended Data Fig.9a). The best docking results obtained from the HDOCK server are shown in Fig.5j. These results confirmed that HDAC11 has a high affinity with the target protein LXRβ.

To determine whether the CALCRL/HDAC11/LXRβ/ABCA1 pathway functions *in vivo*, protein levels of this axis were initially assessed in the hippocampus of mice. As shown in Fig.6k and 6l, Hdac11 protein expression was significantly reduced in *Calca*$^{-/-}$ group. Conversely, *Calca* knockout significantly increased Abca1 protein expression, while having no significant effect on LXRβ protein levels (Fig.6k,l). To further examine whether Abca1 is regulated by Hdac11, immunoprecipitation was performed using Hdac11 antibodies. The results demonstrated that *Calca* knockout disrupted the formation of Hdac11-LXRβ complexes. Additionally, to evaluate whether Hdac11 modulates the acetylation status of LXRβ in mouse brain, protein lysates from the hippocampus were immunoprecipitated with acetylated-lysine antibodies and subsequently analyzed by Western blotting. The findings revealed that *Calca* knockout markedly increased the acetylation of LXRβ. Based on these results, we infer that HDAC11 mediates its effects on AD pathology through the LXRβ/ABCA1 axis.

To verify that HDAC11 is a regulating molecule of the LXRβ/ABCA1 axis in AD pathology, we cultured hippocampal neurons from WT and *Calca*$^{-/-}$ mice, and treated them with 10 μM sAβ1-42 for 24 h. Following sAβ1-42 treatment, Western blot and ELISA analyses revealed no significant increase in α-CGRPlevels in WT neuronal lysates (Extended Data Fig.9b,c). In contrast, a marked elevation of α-CGRP concentration in the supernatant of neuronal cultures was detected by ELISA (Extended Data Fig.9b). Notably, Hdac11 expression was reduced by approximately 50% in the *Calca*$^{-/-}$ group, regardless of sAβ1-42 treatment (Extended Data Fig.9c). Meanwhile, the results of Western blotting and immunofluorescence demonstrated an increase in Abca1 protein expression and a decrease in the BODIPY^{+} dot area in the *Calca*$^{-/-}$ group, irrespective of sAβ1-42 treatment (Extended Data Fig.9c-e). These findings suggest that during the pathological progression of AD, the accumulation of Aβ in neurons may accelerate the release of α-CGRP, which then inhibits LXRβ acetylation via activation of the CALCRL/HDAC11 pathway. Such inhibition of LXRβ acetylation ultimately downregulates Abca1

expression, contributing to lipid metabolism dysregulation. To assess the effects of CGRP on neuronal survival and lipid metabolism, exogenous α-CGRP (0.4 mg/ml) was applied to primary neurons. Although α-CGRP alone had no effect on cell viability, it potentiated Aβ-induced neuronal death, which was rescued by Rim (Extended Data Fig.9f). Meanwhile, α-CGRP promoted lipid accumulation in neurons by enhancing the HDAC11/ABCA1 pathway (Extended Data Fig.9g,h). Although co-treatment with Aβ did not further activate this pathway, it markedly increased lipid accumulation area, which was attenuated by Rim (Extended Data Fig.9g,h). In addition, neurons transfected with siNC or siHdac11 were then treated with either vehicle or sAβ1-42 for 24 hours to mimic physiological and pathological conditions, respectively. As expected, under sAβ1-42 treatment, knockdown of *Hdac11* in neurons enhanced Abac1 expression and reduced lipid accumulation compaired with siNC group (Extended Data Fig.9i,j). To further validate these findings *in vivo*, we performed immunoprecipitation on hippocampal protein lysates from 5×FAD mice infected with rAAV shRNA-Hdac11 or rAAV-GFP, using acetylated-lysine antibodies. The results showed that *Hdac11* knockdown did not alter the expression level of LXRβ but significantly increased its acetylation, which in turn elevated Abca1 protein levels compared with the control group (Fig.6m-p). These findings were further corroborated by immunofluorescence staining of Hdac11 and Abca1 in mouse hippocampus (Fig.6q). Furthermore, Rim treatment also significantly reversed the downregulation of Abac1 protein levels in the hippocampus of 5×FAD mice (Extended Data Fig.9k).

To determine whether microglia are affected by neuronal lipid metabolism, we used siRNA-mediated knockdown of *Hdac11* in primary neurons to simulate neuron–microglia communication observed following in *in vivo* shRNA-Hdac11 knockdown. Microglial BV2 cells treated with conditioned medium from AD like-pathological neurons exhibited elevated HDAC11/ABCA1 pathway activity, lipid accumulation, Nlrp3 expression, and inflammatory factors including iNOS and IL-6. (Extended Data Fig.10a-d). These effects were attenuated when the conditioned medium was derived from *Hdac11*-silenced neurons (Extended Data Fig.10a-d). Given the increased release of CGRP in AD, we further investigated whether microglia respond to CGRP via the Calcrl/Hdac11/Abca1 signaling axis. After treatment with sAβ1-42 (10 μM) for 24 hours, theHdac11/Abca1 pathway was significantly activated, accompanied by lipid accumulation, increased Nlrp3 expression, and elevated levels of inflammatory factors (iNOS, TNF-α and IL-6) (Extended Data Fig.10e-g). In contrast to sAβ1-42 exposure, treatment with α-CGRP alone failed to increase Nlrp3 protein level or the expression of inflammatory mediators (Extended Data Fig.10e-g). Similar to neurons, co-treatment with α-CGRP and sAβ1-42 also did not alter the activity of Hdac11/Abca1 axis in BV2 cells, but exacerbated lipid accumulation, Nlrp3 expression, and IL-6 production (Extended Data Fig.10e-g). Pharmacological inhibition of CGRP receptors using Rim significantly attenuated the cellular phenotypes induced by sAβ1-42 alone or in combination with α-CGRP (Extended Data Fig.10e-g). Moreover, siRNA-mediated knockdown and pharmacological inhibition of Hdac11 by Ele effectively blocked Hdac11-induced Abca1 reduction, lipid accumulation, Nlrp3 upregulation, and proinflammatory cytokine expression (Extended Data Fig.10h-j). These findings confirm the presence of the CALCRL/HDAC11/ABCA1 pathway in microglia and the crosstalk between neurons and microglia in regulating lipid metabolism and inflammation.

To evaluate whether the HDAC11/ABCA1 axis is relevant to humans, we performed Western blot analysis on post-mortem brain samples from individuals with or without dementia. The results demonstrated a significant increase in HDAC11 expression in dementia patients compared with non-dementia controls, accompanied by a marked decrease in ABCA1 expression (Fig.6r-t). Correlation analysis of hippocampal HDAC11 and ABCA1 protein expression levels in both 5×FAD mice and humans revealed a significant negative correlation between these two proteins in both species (Fig.6u). These findings imply that HDAC11 may modulate AD pathology through the LXRβ/ABCA1 axis in mice and humans.

Discussion

In the present study, we observed that the CGRP receptor component CALCRL was highly upregulated in the hippocampal tissues of both AD dementia patients and 5×FAD mice. Inhibition of CGRP receptor function, either through ligand knockout (*Calca*$^{-/-}$) or treatment with the receptor inhibitor Rimegepant (Rim), attenuated sAβ1-42-induced neuronal death in primary cultures and reduced inflammatory responses in glial cells.

Consistent with the *in vitro* findings, *Calca* knockout and chronic Rim treatment in 5×FAD mice alleviated anxiety-like behaviors, improved memory deficits, and mitigated multiple AD-related pathologies, including amyloid plaque deposition, tau hyperphosphorylation and glial activation. These findings indicate that CGRP receptor signaling contributes to AD progression and that its inhibition offers therapeutic benefit. CGRP signaling is well established in migraine pathogenesis through its regulation of inflammation and vasodilation [12,40], and CGRP receptor inhibitors have shown clinical efficacy in reducing migraine frequency and severity [41]. Recent evidence also implicates this pathway in neurodegenerative diseases [42-44]. Consistent with previous studies [44] our findings reinforce the therapeutic potential of targeting CGRP signaling in Alzheimer's disease.

To elucidate the mechanisms underlying Rim's therapeutic effects, we performed bulk RNA-seq and proteomic analyses in the hippocampus of 5×FAD mice. Transcriptomic and proteomic signatures revealed Rim-regulated genes and proteins enriched in immune and inflammatory pathways. Integrated WGCNA and Mfuzz clustering identified 26 overlapping targets, with Hdac11 emerging as a key mediator. As the sole member of the class IV HDAC subfamily, HDAC11 has been implicated in promoting the NLRP3/Caspase-1/IL-1β pathway, which drives inflammation [37]. While HDAC3, HDAC5, and HDAC6 have been reported to play significant roles in AD pathogenesis [34,35,45], currently, evidence linking HDAC11 to AD is rare.

Immunofluorescence staining of the hippocampus in 5×FAD mice and western blotting of primary neurons confirmed that Hdac11 is highly expressed in neurons and selectively responds to Rim treatment. Neuron-specific knockdown of Hdac11 effectively mimicked Rim's protective effects in 5×FAD mice, leading to reductions in Aβ accumulation, tau hyperphosphorylation, glial activation, and cholesterol metabolism dysregulation. Although our findings are consistent with a recent related report [46], the precise role and mechanism of HDAC11 in AD remain unclear. To explore Hdac11's regulatory role

in AD, we identified 154 interacting proteins by IP-MS, revealing associations with neurodegeneration, inflammation, and lipid metabolism. Among 27 potential Hdac11 targets, LXRβ (NR1H2) emerged as a key candidate, as it has been reported to regulate lipid metabolism and inflammation via Abca1, thereby improving cognitive function in AD models [38,39]. In *Calca*$^{-/-}$ mice, Hdac11 expression was reduced while Abca1 expression was elevated. These mice also exhibited decreased formation of Hdac11-LXRβ complexes and enhanced acetylation of LXRβ. Consistent with these findings, Hdac11 inhibition in 5×FAD mice led to increased Abca1 levels and LXRβ acetylation, further supporting the LXRβ/ABCA1 axis in mitigating AD pathology.

Additionally, we found that neurons and microglia share the CALCRL/HDAC11/ABCA1 signaling pathway and engage in crosstalk through lipid metabolism regulation. Conditioned medium from sAβ1-42–treated neurons activated the HDAC11/ABCA1 axis in microglia, promoting lipid accumulation and inflammatory responses. These effects were markedly attenuated when *Hdac11* was knocked down in neurons, indicating functional neuron–microglia crosstalk via this pathway (Extended Data Fig.10k). Moreover, CGRP signaling further amplified Aβ-induced microglial activation, which was reversed by HDAC11 inhibition or CGRP receptor blockade. Notably, this signaling pattern was also observed in human AD brains, supporting the relevance of the HDAC11/LXRβ/ABCA1 axis in AD pathogenesis. Although numerous studies have examined the relationship between microglial lipid metabolism and AD [32,47-52], we propose that microglial lipid perturbations may synergize with neuronal lipid dysregulation and be regulated by neuronal signaling in AD mice.

In conclusion, this study demonstrates that inhibition of CGRP receptor mitigates AD pathology in 5×FAD mice, potentially by reprogramming lipids metabolism via the HDAC11/LXRβ/ABCA1 pathway, a mechanism conserved in humans. Our findings not only elucidate a novel mechanism in AD pathogenesis but also provide compelling evidence supporting the targeting of the CALCRL/HDAC11 axis as a promising therapeutic strategy for AD treatments.

Methods

Mice

C57BL/6Smoc (wild type [WT]) mice and *Calca*$^{-/-}$ mice (C57BL/6Smoc-Calcaem1Smoc, Cat. NO. NM-KO-190928) from Shanghai Model Organisms Center, Inc. (Shanghai, China), and 5×FAD mice (Tg(APPSwFlLon,PSEN1*M146L*L286V)6799Vas, MMRRC stock #34848-JAX) (Oakley et al., 2006) were used for experiments in this study. Genotyping was performed using primers and polymerase chain reaction (PCR) conditions listed on the vendor website (Shanghai Model Organisms Center and JaxLab). The subsequent breeding scheme for 5×FAD mice was consistently that the 5×FAD transgene was derived from paternal inheritance. Male 5×FAD mice and female homozygous Calca-deficient mice were crossbred to generate 5xFAD;Calca KO (homozygotes) mice (referred to as 5xFAD;Calca$^{-/-}$ mice). All animals were maintained on the C57BL/6Smoc background, housed under a 12 h light/12 h dark cycle

with libitum access to food and water. All experiments involving animal procedures were approved by the Institutional Animal Care and Use Committee of Fudan University, Shanghai Medical College.

Caenorhabditis elegans

The C. elegans strains CL2006 (myo-3p::A-Beta (1-42)::let-851 3'UTR)+ rol-6(su1006) and E. coli strain OP50 which were purchased from the Caenorhabditis Genetic Center (University of Minnesota, Minneapolis, MN). CL2006 were maintained at 20 °C, on solid nematode growth medium (NGM) plated with live OP50 as a food source.

Human Subjects

The PART/ABC score distinguishes Primary Age-Related Tauopathy (PART) from Alzheimer's disease by assessing A (amyloid-β deposition, Thal phase 0-5), B (neurofibrillary tangles, Braak stage 0-VI), and C (neuritic plaque density, CERAD score 0-3), where PART is characterized by tau pathology (B) in the absence of amyloid (A0).

For western blotting: hippocampal CA1 samples from adult humans with Alzheimer's disease and age- and sex-matched controls were obtained from Fudan branch of National Health and Disease Human Brain Tissue Resource Center, the Body Donation Station in Fudan University (Shanghai Red Cross Society). Information on the samples are listed in Extended Data Fig.1g. No differences were observed between genders. The use of anonymized excess tissue materials for scientific analyses was approved by the local ethics committee (Research Ethics Committee reference number: 2025-003).

Primary mixglia or neuron culture

For primary mixglial culture, the brains of WT mice at P1-P2 were dissected, and the meninges were removed in Hanks' balanced salt solution (HBSS). The brains were then mechanically dissociated into single-cell suspension within HBSS. After centrifugation, the cells were incubated in Dulbecco 's modified eagle medium (DMEM) containing 10% fetal bovine serum (FBS) in a 25 cm^2 flask with 5% CO_2 at 37 ◦C. The culture media were changed 24 hours later and then twice a week. The AD-like treatment and intervention or medication could be proceeded after 21-day culture.

For primary cortical and hippocampal neuron culture, the pregnant female mice at E15.5-17 were terminally anesthetized with isoflurane. Abdominal skin was washed with 75% ethanol followed by an incision to cut and open the peritoneal cavity. Amniotic sacs were exposed with fine scissors and embryos were taken out from the uterus. The brains of embryos were dissected, and the meninges were removed in HBSS. The tissues were then thoroughly snipped and trypsinized (0.05% trypsin) at 37◦C for 8-10 min to obtain a single cell suspension. The suspension was centrifuged, and the cells were incubated in DMEM containing 10% FBS in a 24-well plate under 5% CO_2 at 37 ◦C. The culture media were changed to Neurobasal containing 2% B27 and 1% GlutaMax 4h later and then half-changed every 72 h. After 7 days, the neurons would be mature enough for experimental use.

BV2 cell line

Microglial BV2 cells were cultured in DMEM containing 10% FBS and 1% Penicillin/Streptomycin under a humidified incubator (5% CO2, 37 ◦C) until use.

Drug treatments

Solutions of Rimegepant (TargetMol Chemicals Inc) were prepared for intraperitoneally (i.p.) injection in mice, following a dosing regimen of 10 mg/kg every other day for a total of 15 doses. sAβ oligomer was produced from β-Amyloid (1-42) (TargetMol Chemicals Inc), which was administrated at a concentration of 10 μM for 24 h in primary cortical neurons from E14.5 embryos and mixglial culture from newborn C57BL/6Smoc or *Calca*$^{-/-}$ mice. Elevenostat (10 μM) (TargetMol Chemicals Inc) was administered via stereotactic injection (1 μL) in 5×FAD mice. All chemical powders were dissolved in DMSO (Beyotime Biotechnology) for storage, except α-CGRP (0.4 mg/mL; TargetMol Chemicals Inc.), which was stored in the appropriate culture medium based on its application.

Preparation of soluble amyloid β 1-42 Oligomers (sAβ1-42)

First, lyophilized synthetic murine Aβ1-42 was dissolved in 100% HFIP (hexafluoroisopropanol) (Sigma-Aldrich) and incubated at room temperature for 1 h to establish randomization of structure formation. The HFIP was evaporated, and the resulting dry peptide was stored at −20 °C. For oligomeric preparation, the peptide was first resuspended in DMSO to a final concentration of 10 mM, then diluted in cell culture medium to a concentration of 1 mM as a storage solution. The solution was incubated at 4 °C for 24 h prior to use.

Molecular docking

The optimized CGRP receptor 3D structure was acquired from PDB database (PDB ID: 3N7R). The pre-processing of the CGRP receptor 3D structure was implemented using Accelrys Discovery studio 2.5 (DS2.5). The docking procedure was implemented using the LibDock program of the DS2.5 simulation software package. The 3D structure of the Hdac11 (AF-Q91WA3-F1) and Nr1h2/LXRβ (AF-Q60644-F1-v4) obtained from AlphaFoldDB (https://alphafold.ebi.ac.uk/) was then minimized on DS2.5. The protein–protein docking simulations were carried out using the HDOCK server. PyMol 1.5 (Schrodinger LLC) was used for visual inspection of the results and graphical representations.

Stereotactic injection of virus and chemicals

Mice were anesthetized with isoflurane and restrained on a stereotaxic apparatus (RWD Life Science) by nose clip and ear bars. Erythromycin ointment (Guangdong Hengjian Pharmaceutical Co., Ltd) was used to moisten the corneal. The scalp was shaved and cleaned, and then a linear incision on the skin was made to expose the skull, which was subsequently cleaned with a cotton swab dipped in normal saline. The brain was adjusted to be flat in both x and y coordinates. According to “The Mouse Brain” (Keith B.J. Franklin and George Paxinos, the third edition, Elsevier), bregma was defined as the origin of stereotaxic

with x = 0, y = 0, z = 0, and lambda was defined as x = 0, y = −4.2 mm, z = 0. If the distance between bregma and lambda was not 4.2 mm, the coordinates for the injection site were calculated proportionally. The skull above the target area was drilled open and a glass pipette (WPI, pulled by Sutter PC-10, NARISHIGE) was inserted into the injection site.

rAAV-hSyn-EGFP-5'miR-30a-shRNA(Hdac11)-3'-miR30a-WPREs [5×10^{12} viral genome (v.g.)/mL] and rAAV-hSyn-EGFP-5'miR-30a-shRNA(scramble)-3'-miR30a-WPREs (5×10^{12} v.g./mL) were produced by BrainVTA Co.,Ltd (Wuhan, China), and aliquoted and stored at 80 ℃ until use.

300 nL rAAV or 1 μL Elevenostat (10 μM) were bilaterally injected into CA1 regions of 5×FAD mice (AP, -2.00 mm from bregma; ML, ± 1.60 mm; DV, - 1.90 mm from the skull) at the rate of 80 nL/min for each site. After injection, the glass pipette was pulled out slowly after 10-min staying.

Paralysis time assay

Paralysis assay was performed in CL2006 worms to assess the effect of Rimegepant and Elevenostat on delaying the onset of amyloid-β-induced paralysis. Petri dishes (6cm) containing Nematode Growth Medium (NGM) were supplemented with Rimegepant at concentrations of 0.4 μM, 2 μM, or 10 μM, or Elevenostat at 4 μM, 20 μM, or 100 μM. After the agar had solidified, the compounds were allowed to diffuse throughout the agar and incubated at room temperature for 30 minutes. The Petri plates were then kept at 16 °C overnight and seeded with 50 μL OP50 (0.5 mg/mL) as previously described.

Open field test (OF)

The animal spontaneous locomotor activity was measured in a plexiglass box (42×42×50cm), recorded by Ethovision XT14.0 software (Noldus). During testing, mice were placed in the center of the activity chamber and allowed to freely explore for 10 min, not affected by external stimuli. Anxiety-related performance was quantified by calculating the number of times entering the central area. The time spent in the center of the box (half of the box area) was also recorded.

Novel location recognition test (NLR) and Novel object recognition test (NOR)

The novel location recognition test or novel object recognition test was performed in an open field where the movements of mice were recorded via a camera mounted above the field. Before each test, mice were acclimatized in the behavioral room for 30 min and were given a 10 min habituation trial with no objects on the open field.

First, each mouse was placed on one side of the open field and allowed to explore freely for 10 minutes. After one day, two identical objects were presented to the mouse for 10 min. The following day, one object was relocated to a novel position, and the mouse was allowed to explore for 10 min. On the subsequent day, one object was replaced with a novel object, and the mouse was given 10 min to explore. The chamber and objects were cleaned with 75% ethanol between trials to remove olfactory stimuli. Testing sessions were video monitored, and object exploration times were scored by a blinded

experimenter. The results were quantified as the frequency of exploration for the novel object compared with the total frequency of novel and familiar object or location.

Y-maze test

The Y-maze apparatus was made of acrylic plastic and was either black or gray in color. Mice were placed in the center of the Y-shaped maze, which consisted of three equal arms (A, B, C), each measuring 50 cm x 10 cm. Mice were allowed to explore the maze for 10 min, and the number and sequence of entries into the different arms were recorded. Three consecutive entries into different arms were considered one alternation. Percentage of alternation was calculated as follows: number of triads containing entries into 3 different arms/(total number of arms entered −2) × 100%. After each test, the mouse was carefully removed from the maze, and the maze was cleaned with 75% ethanol followed by distilled water. All other experimental conditions were kept consistent between the group.

Elevated plus maze test (EPM)

The elevated plus maze consists of two open arms (without walls, 35 cm long X 6 cm wide) and two closed arms (with walls 19 cm tall), the intersection of the arms is 6 cm x 6 cm wide, and the entire maze is elevated 73 cm above the ground. Mice were first allowed to habituate in the testing room under dim light for 1 h prior to the start of testing. During testing, mice are placed in the maze at the intersection of the open and closed arms and allowed to freely explore the maze for 10 min. The maze is cleaned with 75% alcohol between testing of each mouse. The anxiety index was measured as follows: 1 − [(time spent in open arm (OA)/total time on the maze) + (number of entries to the OA/total exploration on the maze)/2] [53].

Forced swimming test (FST)

Forced swimming test was also for assessing depressive-like behavior. Each mouse was placed individually into glass cylinders. The test lasted for 6 min and the activity of mouse was video-recorded for analysis. Immobility was defined as the absence of any movement except for the head above water.

Morris water maze test (MWM)

Mice were trained to search an unhidden circular escape platform (10 cm) in a pool (120 cm diameter) filled with opaque water by using different cues. The pool was filled with tap water mixed with non-toxic white paint. During the whole test the water temperature was maintained at 20 ± 2 °C. The pool was divided into four virtual quadrants based on the platform localization: left, right, opposite, and target.

Each mouse went through 5 or 6 days of acquisition training and a final probe trial. During the acquisition training, the platform was not hidden under the water. Mice were introduced into the water near the edge of the pool facing the wall. They were given one minute to find the submerged platform. The platform was located in the upper third of the quadrant (10 cm from the rim of the pool). If they failed to find the platform in one minute, they were gently guided to it. Every mouse had to sit on the platform for 15 s

before being removed from the pool. To prevent hypothermia mice were kept in front of a heat lamp until they were dry. The cued training consisted of four trials per day with an average inter-trial interval of 60 min. The start position changed for every trial with the stationary location of platform. Twenty-four hours after the last acquisition trial, a probe trial was performed to assess spatial reference memory. For the probe trial the platform was removed from the pool, and mice were introduced into the water from a novel entry point (opposite of the platform location). Mice were allowed to swim freely for one minute. To calculate the time to reach the target, the position of the platform in the tracking software was set to the same position as in the previous acquisition training. For tracking the learning curve in training phases, platform crossing number, and percentage time spent in target quadrant, Ethovision XT14 video tracking software (Noldus) was used.

Immunohistochemistry and immunofluorescence microscopy

Brain tissue/slices were post-fixed in 4% PFA in PBS at 4 °C overnight then subsequently transferred into 20% and then 30% sucrose solution until cryo-sectioning. After embedding in optimal cutting temperature (OCT) compound, the slices were further cut coronally or sagittally into 30-µm-thick sections on a cryostat (Leica Biosystems). For immunofluorescence (IF) staining, 30 µm thick free-floating brain sections or sections mounted on glass slides were washed, blocked and permeabilized by incubating in PBS containing 0.30% Triton X-100 and 5% goat or donkey serum for 1h in thermostat water bath or incubator at 37 °C. Primary antibodies were diluted in PBS containing 0.30% Triton-X-100 and 1% goat or donkey serum. After overnight incubation at 4 °C with primary antibodies, the sections were rinsed 3x in PBS at room temperature for 5 min each. Then, the sections were incubated in the appropriate fluorophore-conjugated secondary antibody at room temperature for 1.5-2 h in the dark. The sections were rinsed once and incubated with DAPI (1µg/ml) for 10min, washed 3x in PBS for 10 min, dried, and cover slipped with ProLong Diamond Antifade Mountant (Thermo Fisher).

Thioflavin-S and BODPIY staining

For Aβ plaques staining, briefly deparaffinized and rehydrated slides were incubated for 10 min in 1% thioflavin-S (Sigma) which was dissolved in 50% ethanol and the slides were subsequently rinsed in 80% ethanol and 50% ethanol.For detecting lipid droplets, BODIPY™ 493/503 (Thermo Fisher) was dissolved in PBS to prepare a 10 µM working solution.

Image Acquisition and Analysis

Sections were imaged using a Nikon AIR-MP confocal microscope (Japan). $GFAP^+$ and $IBA1^+$ cells in the cortex and hippocampus were quantified using ImageJ. Regions of interest (ROIs) were manually outlined, and a consistent threshold above background was applied to segment positive signals. Manual counting of immunopositive cells was performed on each image. For quantification of plaque-associated DAA and DAM, brain sections were immunostained with 6E10 (Aβ), GFAP, and IBA1. Aβ plaques were identified by 6E10 staining, and circular ROIs (50 µm radius) were drawn around each plaque. Cell counts were normalized to the ROI area and reported as cells per mm^2. Quantification was performed on two to

three brain sections per mouse, and the final value for each mouse was represented as the average from these sections., analyzing 60 IBA1$^+$ microglia per mouse. The final value for each group represents the average of these cells per mouse. A similar approach was used to quantify the number of Thioflavin-S$^+$ plaques and Nissl-positive neuron.

IMARIS software with SURFACE and COLOCALIZE Functions was used for quantification of CD11b$^+$ and C3$^+$ signals within glial cells. Quantification was performed on two to three brain sections per mouse, and the final value for each mouse was represented as the average from these sections.

For immunohistochemically stained microglia. ROIs were manually selected in the cortex and hippocampus. Cell boundaries were delineated based on IBA1$^+$ immunoreactivity using ImageJ. The area of individual microglial cells was measured using the “Analyze Particles” function after appropriate thresholding. Measurements were averaged from multiple cells per animal across 2–3 brain sections. Quantification was performed on two to three brain sections per mouse, with 60 IBA1$^+$ microglia randomly selected and analyzed per mouse.

Z-stack confocal images were acquired and analyzed using ImageJ to quantify lipid accumulation. IBA1$^+$ microglia were identified manually or with the Spots function. BODIPY$^+$ lipid signals within IBA1$^+$ cells were detected by applying a consistent threshold determined by visual inspection and uniformly applied across all images. For each z-stack, the percentage of BODIPY$^+$ signal area relative to the IBA1$^+$ cell area was calculated on a per-cell basis. Quantification was performed on 2–3 brain sections per mouse, with 60 BODIPY$^+$/IBA1$^+$ microglia randomly selected and analyzed per mouse. The final value for each group represents the average of these cells per mouse. A similar approach was used to calculate the percentage of BODIPY$^+$ signal coverage over the NeuN$^+$/MAP2$^+$ neuron area or IBA1$^+$ microglial BV2 cells. Specifically, 30 NeuN$^+$/MAP2$^+$ neurons were randomly selected from each neuronal group for quantification. For microglia, several hundreds of IBA1$^+$ cells from 5 images per well for 2-3 wells were analyzed per group for quantification. Data represent the mean values averaged over three independent experiments.

Fluorescence intensity was quantified using ImageJ. ROIs were manually drawn around individual NeuN$^+$/Abac1$^+$ cells. The mean fluorescence intensity within each ROI was measured. Background intensity was measured from adjacent unstained areas and subtracted from the raw values. Quantification was performed on at least 30 cells per group. The final values represent the average intensity per cell, averaged across three independent experiments.

All analyses were performed blinded to treatment and genotype.

Scanning electron microscopy

The samples for scanning electron microscopy (SEM) analysis were prepared using the following method: 100 μL of sAβ1-42 (1 mM) was centrifuged at 13,000g for 5 min and then applied to the

polished surface of a silicon wafer and air-dried. The samples were analyzed using a desktop field-emission SEM (Phenom Pharos-SED-EDS G2, Thermo Fisher) at an acceleration voltage of 10 kV.

In vitro siRNA mediated Hdac11 knockdown

siRNA targeting Hdac11 (siHdac11) was purchased from Tsingke (target sequences: 5'-GACAAGCGAGUAUACAUCA-3'; 5'-UGAUGUAUACUCGCUUGUC-3'). Negative control siRNA (siNC) was also purchased from Tsingke (target sequence: 5'-UAGCGACUAAACACAUCAA-3'). Transfection reagent Lipofectamine 2000 were purchased from Invitrogen (Carlsbad, USA).

Cell viability assays

Cell viability was assessed using the Cell Counting Kit-8 (CCK-8) (Beyotime) and Hoechst 33342/PI double staining kit (Beyotime). Briefly, cells were seeded in 96-well or 24-well plates and allowed to grow to 80% confluence. Cells were then treated with sAβ1-42 (10 μM) with or without various doses of Rim or Ele for 24 h, with sAβ1-42 vehicle as the control. Cell viability was determined using CCK-8 and Hoechst 33342/PI staining according to the manufacturer's instructions.

Western blotting

Total protein was extracted from cultured cells and tissues using RIPA Lysis Buffer (Beyotime) supplemented with protease inhibitor cocktail (Beyotime). The protein samples were then separated by SDS-PAGE and transferred onto PVDF membranes (Millipore). For HRP-conjugated secondary antibodies, proteins were detected using the enhanced chemiluminescence method (ECL) (BioRad). The quantification of each band was performed by densitometric measurement using ImageJ software. The list of antibodies used is provided in Supplementary Table 2.

Immunoprecipitation and Immunoblotting

Immunoprecipitation (IP) assays were performed using the Pierce™ Classic Magnetic IP/Co-IP Kit (Thermo Fisher), following the manufacturer's protocol. Briefly, hippocampal tissue was lysed in RIPA Lysis Buffer (Beyotime) for 20 min on ice. The cell lysates were then centrifuged at 13,000 rpm for 15 min, and the supernatants were incubated overnight with Anti-HDAC11 antibody or Anti-acetyl-Lysine antibody. After overnight incubation, protein A/G magnetic beads (washed three times with IP Lysis/Wash Buffer) were added to the cell extracts and incubated with gentle shaking for 1 hour at room temperature. The beads were then washed three times with IP Lysis/Wash Buffer, resuspended in 50 μL of SDS sample buffer, and boiled at 97 °C for 10 min. The immunoprecipitates were subsequently analyzed by standard immunoblotting.

ELISAs for α-CGRP and Aβ40-42

Primary cortical neurons were prepared as described in the Primary Microglia and Cortical Neuron Culture section. Briefly, cells were seeded in 24-well plates and allowed to grow to 80% confluence. Cells

were then treated with sAβ1-42 (10 μM), with the sAβ1-42 vehicle used as the control. After determining total protein concentrations using the BCA assay, the concentration of α-CGRP in both the supernatant and cell lysates was measured by using an ELISA kit for α-CGRP (Cloud-Clone Corp), following the manufacturer's protocol.

Hippocampus and cotex were prepared for the insoluble and soluble Aβ40-42 extraction following the procedures as described [54]. Briefly, both tissues were homogenized in TBS containing Protease and Phosphatase Inhibitor Cocktail. Prepared brain tissue homogenates were thawed on ice and centrifuged at 14,000g for 30 min at 4 °C. The supernatant was collected as the TBS soluble fraction. The remaining pellet was resuspended in ice-cold 70% formic acid-containing Protease and Phosphatase Inhibitor Cocktail, sonicated on ice six times for 10 s and centrifuged at 14,000g for 1 h at 4 °C. The supernatant was collected as the formic acid-soluble fraction, neutralized 1:20 in 1 M Tris-base at room temperature. After extraction, the concentrations of insoluble and soluble Aβ40-42 in both regions were measured by using ELISA Kits for either Amyloid Beta Peptide 1-40 (Ab1-40) or Amyloid Beta Peptide 1-42 (Ab1-42) (Cloud-Clone Corp), following the exact manufacturer's insructions.

Data analysis of snRNA-seq datasets

snRNA-seq dataset (GSE148822) contains 18 samples including 482,472 sequenced nuclei with 10 AD samples including 3 male and 7 female AD donors, 5 control without amyloid plaques (CTR) samples and 3 control plus amyloid plaques (CTR+) samples. The expression matrix was imported into R (version 4.3.1) using the Seurat package (version 2.3.4). Default parameters within the Seurat package were employed unless otherwise specified. Cells were excluded if they exhibited fewer than 200 or more than 5000 genes, or if more than 10% of their expressed genes were mitochondrial, to ensure that only cells in good condition and without doublets were included. After independent normalization of the data, we merged the patient and control expression matrixes using Seurat built-in function called “Run Harmony”. This was followed by scaling the matrix and performing principal component analysis (PCA) based on the top 2000 highly variable genes. The top 11 principles were employed to construct uniform manifold approximation and projection (UMAP).

RNA extraction, RT-qPCR and RNA-seq

Total RNA was extracted from cultured cells and the tissues using TRIzol reagent (TIANGEN), following the manufacturer’s protocol. Reverse transcription was carried out using random primers and the Fastking gDNA Dispelling RT SuperMix (TIANGEN). Quantitative real-time PCR using the SuperReal PreMix Plus (SYBR Green) (TIANGEN). For primer sequences see Key Resources.

For RNA-seq, the quality of the total RNA was first assessed. Then, the library was constructed, purified, detected and quantified. Following the generation of sequencing clusters, sequencing was conducted on the Illumina/MGI platform. The list of primers used is provided in Supplementary Table 3.

Single cell sample preparation

Frozen hippocampi from 3 mice of the same genotype/treatment were pooled as a single sample. Tissue was homogenized with Dounce homogenizer in lysis buffer (10mM Tris-HCl, pH 7.4, 10mM NaCl, 3mM $MgCl_2$, 0.005% NP-40, 0.2 U/ul RNAase Inhibitors in nuclease-free water), and incubated on ice for 15 min. The single-cell suspensions were filtered through a 70-μm and 30-μm cell strainer (Miltenyi Biotech, PN:130-098-458 and 130-098-462), and then treated with the Red Blood Cell Lysis Solution (Miltenyi Biotech, PN:130-094-183). The viability of cells was determined by using Countstar Rigel (Alit Biotech), and dead cell removal was carried out depending on the viability using the Dead Cell Removal Kit (Miltenyi Biotech, PN:130-090-101). Finally, the cells were re- suspended in 1x PBS (Invitrogen) supplemented with 0.04% BSA at a final concentration of 700-1200 cells/μL, and were then processed with the 10x Chromium Single Cell 3’ Kit (v3.1 PN:1000268 or v4 PN:1000691, depends on project) as per the manufacturer's instructions at Hangzhou Cosmos Wisdom

Single-cell 3’ RNA sequencing

The cell suspension was loaded into 10x Chromium Chip (v3.1 PN:1000120 or v4 PN:1000690, depends on project) and barcoded with a 10x Chromium Controller (or Chromium X, depends on project). RNA from the barcoded cells was subsequently reverse-transcribed, amplified and prepared into sequencing libraries with 10x Library Construction Kit (v3.1 PN:1000190 or v4 PN:1000694) according to the manufacturer’s instructions. Sequencing was performed with Illumina NovaSeq (or GeneMind SURFSeq 5000, depends on project) with 150-bp paired-end reads at Hangzhou Cosmos Wisdom Biotech Co.,Ltd. (Hangzhou,China).

We use fastp (v0.20.0) software to perform basic quality statistics on the raw reads. Generally, the 10x Genomics® Cell Ranger software supports FASTQ files generated directly from raw base call (BCL) files by Illumina sequencers as input and not recommend additional sequence processing.

If clean reads are indispensable for the analysis:

Then, raw read sequences produced by the Illumina pipeline in FASTQ format were pre-processed using fastp (v0.20.0) software with the following steps:

(1) 3' End Trimming: Remove low-quality bases from the 3' end towards the 5' end using a sliding window of size 1 base. Bases within the window are removed if the mean base quality score in the window is < 3 (Parameters: --cut_tail --cut_tail_window_size 1 --cut_tail_mean_quality 3).

(2) 5' End Trimming: Remove low-quality regions starting from the 5' end towards the 3' end. A sliding window of size 4 bases is moved from the 5' end. When a window with a mean base quality score < 10 is encountered, the bases within that window and all subsequent bases to the right (3' end)

are removed (Parameters: --cut_right --cut_right_window_size 4 --cut_right_mean_quality 10).

(3) Read Length Filtering: Discard reads shorter than 28 bases (Parameters: --length_required 28).

(4) Paired-End Read Integrity: Discard reads that cannot form proper pairs (i.e., unpaired reads).

The remaining reads that passed all the filtering steps were designated as clean reads. All subsequent analyses were based on these clean reads. Finally, we use fastp (v0.20.0) software to perform basic statistics on the quality of the clean reads.

Data processing with Seurat package

The expression matrix was imported into R using the Seurat package. Default parameters within the Seurat package were employed unless otherwise specified. Cells were excluded if they exhibited fewer than 200 or more than 5000 genes, or if more than 10% of their expressed genes were mitochondrial, to ensure that only cells in good condition and without doublets were included. This was followed by scaling the matrix and performing PCA based on the top 2000 highly variable genes. The top 20 PCs were selected for downstream cluster identification and visualization. Using the “Find Clusters” function, we identified 18 clusters at a resolution of 0.5. The top 18 principles were employed for the construction of UMAP.

Cell–cell communication analysis was performed using the CellChat R package (version 1.6.1). Genes were first filtered and normalized according to CellChat's standard workflow. We employed the built-in ligand–receptor interaction database for mouse provided by CellChat. The communication probability between cell clusters was inferred based on known ligand–receptor pairs, and the overall communication network was visualized using netVisual_circle functions.

Gene set variation analysis (GSVA) was performed using the GSVA package (version 1.50.0). The GSVA score for each cluster was calculated as the average normalized expression of genes associated with the specified pathway.

RNA-seq

After quality control, the raw data were aligned to the mice reference genome. Differential expression analysis was performed using the and Limma (3.58.1) R package. adj. *p* value <= 0.05 was set as the threshold for significantly differential expression. GOseq was employed to analyze the GO enrichment of the differentially expressed genes in molecular function, cellular component, and biological process, and the criteria for screening significant enrichment were over represented adj. *p* value <= 0.05. GSEA was performed using the “GSEA” R package. analysis was WGCNA analysis was realized with R package “WGCNA” (version 1.68). The clustering of the genes was performed with “Mfuzz” R package.

Protein digestion and desalination

Using QLBIO MAGicomicomicS-MMB8X, 20 µL of protein was added to eight tandem tubes containing MMB beads and incubated at 37 °C for 30 min. After incubation, 45 µL of bonding solution was added and incubated at room temperature for 15 min. Following this, the supernatant was discarded, and the MMB beads were washed three times with cleaning solution. The magnetic beads were then re-

suspended in 40 μL of enzyme working solution and incubated at 37 °C for over 4 h. After incubation, 5 μL of termination solution was added to halt the enzyme reaction, and the mixture was freeze-dried.

LC-MS/MS analysis

Nanoflow LC-MS/MS analysis of tryptic peptides was performed on a quadrupole Orbitrap mass spectrometer (Thermo Fisher) coupled to an EASY nLC 1200 ultra-high pressure system (Thermo Fisher) via a nano-electrospray ion source. One microgram of peptides was loaded onto a 25 cm column (100 μm inner diameter, packed with ReproSil-Pur C18-AQ 1.5-μm silica beads; QL-HPLC-100*15; Beijing Qinglian Biotech Co., Ltd). Peptides were separated using a gradient: 8–12% B in 2min, followed by 12–30% B in 3min, and then increased to 40% B in 7min, followed by a 10min wash at 95% B at a flow rate of 300nL per minute. Solvent A was 0.1% formic acid in water, and solvent B was 80% acetonitrile (ACN) with 0.1% formic acid in water. The total run duration was 30 min. The column temperature was maintained at 60 °C using an in-house-developed oven. The mass spectrometer was operated in “top-40” data-dependent mode, collecting MS spectra in the Orbitrap mass analyzer (120,000 resolution, 350–1500 m/z range) with an automatic gain control (AGC) target of 3E6 and a maximum ion injection time of 80 ms. The most intense ions from the full scan were isolated with an isolation width of 1.6m/z. Following higher-energy collisional dissociation (HCD) with a normalized collision energy (NCE) of 27, MS/MS spectra were acquired in the Orbitrap (15,000 resolution) with an AGC target of 5E4 and a maximum ion injection time of 45 ms. Precursor dynamic exclusion was enabled with a duration of 16s.

The identification and quantitation of protein

All raw files were analyzed using the Proteome Discoverer suite (Thermo Fisher). MS2 spectra were searched against the UniProtKB human proteome database, including Swiss-Prot human reference protein sequences. The Sequest HT search engine was used, with the following parameters: fully tryptic specificity, a maximum of two missed cleavages, a minimum peptide length of 6, fixed carbamidomethylation of cysteine residues (+57.02146 Da), variable oxidation of methionine residues (+15.99492 Da), a precursor mass tolerance of 15 ppm, and a fragment mass tolerance of 0.02 Da for MS2 spectra collected in the Orbitrap. A Percolator was used to filter peptide spectral matches and peptides to a false discovery rate (FDR) of less than 1%. After spectral assignment, peptides were assembled into proteins, which were further filtered based on the combined probabilities of their constituent peptides, maintaining a final FDR of 1%. By default, the top matching protein, or ‘master protein,’ is the protein with the largest number of unique peptides and the smallest value in percent peptide coverage (i.e., the longest protein). Only unique and razor (i.e., parsimonious) peptides were considered for quantification.

Tissue lipid extraction

Forty microliters of cold water were added to accurately weigh 10 ± 0.2 mg of hippocampal tissue, followed by homogenization at 20 Hz for 2 min. Next, 20 μL of the supernatant was removed, and 225 μL of MeOH was added, followed by vortexing for 10 s. Then, 5 μL of the internal standard and 750 μL of

MTBE were added, and the mixture was vortexed for 10 seconds both before and after adding MTBE. The mixture was then incubated for 30 min, followed by the addition of 188 μL of H_2O and vortexing for 10 s to form a two-phase system. After equilibration for 10 min at 4 °C, the mixture was centrifuged at 10,000g for 10 min at 4 °C. Seven hundred microliters of the supernatant were dried under nitrogen. All samples were reconstituted in ACN/IPA/H_2O (65:30:5, v/v/v), and 20 μL of the mixture was used as a quality control (QC) sample. Finally, 2 μL of each sample was injected into the LC-MS system.

Proteomics analysis

Total protein from mouse hippocampal tissues was extracted. Proteins were labeled with iTRAQ labeling reagents (ABSCIEX, 4,381,663) and then subjected to Liquid Chromatography and tandem MS analysis. Protein analysis and relative iTRAQ quantification services were undertaken by OE Biotech. Differentially expressed protein (DEP) was performed using the DESeq and Limma R package. adj. *p* value <= 0.05 was set as the threshold for significantly differential expression. “KEGG” R package was used for KEGG pathway enrichment analyses of DEPs. The clustering of the proteins was performed with “Mfuzz” R package.

Lipidomics

Lipidomic profiling was performed using an Ultra-Performance Liquid Chromatography-Mass Spectrometry (UPLC-MS/MS) system (UPLC, Agilent 1290; MS, Applied Biosystems SCIEX 6500+QTRAP) at the Core Facility of Basic Medical Sciences, Shanghai Jiao Tong University School of Medicine (Shanghai, China). The samples were separated using reverse-phase chromatography (Kinetex® 2.6 μm C18, 2.1 × 100 mm, Phenomenex). The experiment was conducted in Multi-Reaction Monitoring (MRM) mode, with each lipid type calibrated using corresponding lipid isotope standards to ensure experimental accuracy. Mass spectrometric data were processed using Analyst 1.6.3 software (AB Sciex). Data processing involved Sciex OS software, and the analytical data consisted of retention time (RT), normalization by internal standards (ISTDs), and baselining towards blank runs to remove background noise. After PCA, differential expression analysis was performed using the DESeq (2012) R package. adj. *p* value <= 0.05 was set as the threshold for significantly differential expression.

Statistics and reproducibility

R studio (4.3.1) and GraphPad Prism (v.8.0) software was used for statistical analyses. Data are presented as mean ± standard error of the mean (SEM), unless otherwise specified. All statistical tests were two-tailed, and replicates represent biological replicates unless otherwise stated. P values were calculated using two-sided Student’s t-tests for measurements for comparisons between two groups, unless indicated otherwise in the figure legends. One-way analysis of variance (ANOVA) with post hoc Dunnett’s test was used for comparisons among several groups, and two-way ANOVA followed by Bonferroni multiple comparisons was used for analyses involving several groups. Statistical tests used for each experiment are indicated in the corresponding figure legends. A P value less than 0.05 was considered statistically significant. Western blot experiments were replicated at least three times with

reproducible results. All in vitro assays were performed at least three times with a minimum of n = 3 biological replicates per group. For in vivo experiments, the minimum sample size was three independent mice, with exact sample sizes per condition reported in the figure legends. Spearman method was used for the correlation analysis. Individual data points are shown as one dot per sample. Samples and experimental animals were randomly assigned to experimental groups, and sample collection was performed randomly when possible.

Declarations

Acknowledgements

We thank Meng Liu from the Core Facility of Basic Medical Sciences, Shanghai Jiao Tong University School of Medicine, for their invaluable contribution to the lipidomic analysis in this study.

Author contributions

F.H., R.S., J.F., W.L. and M.Y. proposed and supervised the study. G.F. and F.C. performed most experiments and analyzed the data, with assistance from M.L., P.Y., H.D., J.S., M.W., Z.W., P.N., C.S., X.T., X.Y., H.L., J.Z., Y.Z., Z.C., H.L., X.L., R.Z., Y.L., L.C.. All authors contributed to the interpretation of data and the revision of the manuscript.

Competing interests

Authors listed declare that they have no competing interests.

Correspondence

Correspondence to Mei Yu, Wensheng Li, Jian Fei, Ruling Shen and Fang Huang.

Data availability

All data reported in this paper will be shared by the lead contact upon request.

References

1. Selkoe, D. J. & Hardy, J. The amyloid hypothesis of Alzheimer's disease at 25 years. *EMBO molecular medicine* **8**, 595-608 (2016).
2. Tzioras, M., McGeachan, R. I., Durrant, C. S. & Spires-Jones, T. L. Synaptic degeneration in Alzheimer disease. *Nature Reviews Neurology* **19**, 19-38 (2023).
3. Brain, S. D. & Grant, A. D. Vascular actions of calcitonin gene-related peptide and adrenomedullin. *Physiological reviews* **84**, 903-934 (2004).
4. Russell, F. A., King, R., Smillie, S.-J., Kodji, X. & Brain, S. Calcitonin gene-related peptide: physiology and pathophysiology. *Physiological reviews* **94**, 1099-1142 (2014).

5. Zhao, X., Wu, G., Zhang, J., Yu, Z. & Wang, J. Activation of CGRP receptor–mediated signaling promotes tendon-bone healing. *Science Advances* **10**, eadg7380 (2024).
6. Zhi, X. *et al.* Nociceptive neurons promote gastric tumour progression via a CGRP–RAMP1 axis. *Nature* **640**, 802-810 (2025).
7. McLatchie, L. M. *et al.* RAMPs regulate the transport and ligand specificity of the calcitonin-receptor-like receptor. *Nature* **393**, 333-339 (1998).
8. Edvinsson, L., Haanes, K. A., Warfvinge, K. & Krause, D. N. CGRP as the target of new migraine therapies—successful translation from bench to clinic. *Nature Reviews Neurology* **14**, 338-350 (2018).
9. Hay, D. L. & Walker, C. S. CGRP and its receptors. *Headache: The Journal of Head and Face Pain* **57**, 625-636 (2017).
10. Lelkes, Y., Sood, G. & Iyengar, S. The hostile audience: The effect of access to broadband internet on partisan affect. *American Journal of Political Science* **61**, 5-20 (2017).
11. Edvinsson, L., Haanes, K. A. & Warfvinge, K. Does inflammation have a role in migraine? *Nature Reviews Neurology* **15**, 483-490 (2019).
12. Ho, T. W., Edvinsson, L. & Goadsby, P. J. CGRP and its receptors provide new insights into migraine pathophysiology. *Nature Reviews Neurology* **6**, 573-582 (2010).
13. Kaag Rasmussen, M. *et al.* Trigeminal ganglion neurons are directly activated by influx of CSF solutes in a migraine model. *Science* **385**, 80-86 (2024).
14. Song, Y. *et al.* Neuron-glia crosstalk and inflammatory mediators in migraine pathophysiology. *Neuroscience* **560**, 381-396 (2024).
15. Wen, Q. *et al.* MicroRNA-155-5p promotes neuroinflammation and central sensitization via inhibiting SIRT1 in a nitroglycerin-induced chronic migraine mouse model. *Journal of neuroinflammation* **18**, 287 (2021).
16. Tsuru, S. *et al.* RAMP1 signaling in immune cells regulates inflammation-associated lymphangiogenesis. *Laboratory investigation* **100**, 738-750 (2020).
17. Lu, Y.-Z. *et al.* CGRP sensory neurons promote tissue healing via neutrophils and macrophages. *Nature* **628**, 604-611 (2024).
18. Heneka, M. T. *et al.* Neuroinflammation in Alzheimer's disease. *The Lancet Neurology* **14**, 388-405 (2015).
19. Scheiblich, H. *et al.* Microglia rescue neurons from aggregate-induced neuronal dysfunction and death through tunneling nanotubes. *Neuron* **112**, 3106-3125. e3108 (2024).
20. Gabitto, M. I. *et al.* Integrated multimodal cell atlas of Alzheimer’s disease. *Nature Neuroscience* **27**, 2366-2383 (2024).
21. Jorstad, N. L. *et al.* Comparative transcriptomics reveals human-specific cortical features. *Science* **382**, eade9516 (2023).

22. Gerrits, E. *et al.* Distinct amyloid-β and tau-associated microglia profiles in Alzheimer's disease. *Acta neuropathologica* **141**, 681-696 (2021).
23. Mhillaj, E. *et al.* Celecoxib prevents cognitive impairment and neuroinflammation in soluble amyloid β-treated rats. *Neuroscience* **372**, 58-73 (2018).
24. Khurana, V. *et al.* TOR-mediated cell-cycle activation causes neurodegeneration in a Drosophila tauopathy model. *Current Biology* **16**, 230-241 (2006).
25. Leng, F. & Edison, P. Neuroinflammation and microglial activation in Alzheimer disease: where do we go from here? *Nature Reviews Neurology* **17**, 157-172 (2021).
26. Kwon, H. S. & Koh, S.-H. Neuroinflammation in neurodegenerative disorders: the roles of microglia and astrocytes. *Translational neurodegeneration* **9**, 42 (2020).
27. Mullin, K. *et al.* Potential for treatment benefit of small molecule CGRP receptor antagonist plus monoclonal antibody in migraine therapy. *Neurology* **94**, e2121-e2125 (2020).
28. Kaji, S. *et al.* Apolipoprotein E aggregation in microglia initiates Alzheimer's disease pathology by seeding β-amyloidosis. *Immunity* **57**, 2651-2668. e2612 (2024).
29. Li, J. H., Hepworth, M. R. & O'Sullivan, T. E. Regulation of systemic metabolism by tissue-resident immune cell circuits. *Immunity* **56**, 1168-1186 (2023).
30. Wang, Z., Zhang, L. & Qin, C. Alzheimer's disease pathogenesis: standing at the crossroad of lipid metabolism and immune response. *Molecular Neurodegeneration* **20**, 67 (2025).
31. Ferré-González, L. *et al.* Brain areas lipidomics in female transgenic mouse model of Alzheimer's disease. *Scientific reports* **14**, 870 (2024).
32. Litvinchuk, A. *et al.* Amelioration of Tau and ApoE4-linked glial lipid accumulation and neurodegeneration with an LXR agonist. *Neuron* **112**, 384-403. e388 (2024).
33. Shen, C. *et al.* HDAC inhibitors enhance the anti-tumor effect of immunotherapies in hepatocellular carcinoma. *Frontiers in immunology* **14**, 1170207 (2023).
34. Agis-Balboa, R. C., Pavelka, Z., Kerimoglu, C. & Fischer, A. Loss of HDAC5 impairs memory function: implications for Alzheimer's disease. *Journal of Alzheimer's disease* **33**, 35-44 (2012).
35. Ricciardi, N. R. *et al.* Investigating the synergistic potential of low-dose hdac3 inhibition and radiotherapy in alzheimer's disease models. *Molecular neurobiology* **60**, 4811-4827 (2023).
36. Zhang, L., Sheng, S. & Qin, C. The role of HDAC6 in Alzheimer's disease. *Journal of Alzheimer's disease* **33**, 283-295 (2012).
37. Yao, F. *et al.* HDAC11 promotes both NLRP3/caspase-1/GSDMD and caspase-3/GSDME pathways causing pyroptosis via ERG in vascular endothelial cells. *Cell Death Discovery* **8**, 112 (2022).
38. Kang, J. & Rivest, S. Lipid metabolism and neuroinflammation in Alzheimer's disease: a role for liver X receptors. *Endocrine reviews* **33**, 715-746 (2012).
39. Lewandowski, C. T., Laham, M. S. & Thatcher, G. R. Remembering your A, B, C's: Alzheimer's disease and ABCA1. *Acta Pharmaceutica Sinica B* **12**, 995-1018 (2022).

40. Malhotra, R. Understanding migraine: Potential role of neurogenic inflammation. *Annals of Indian Academy of Neurology* **19**, 175-182 (2016).
41. Dodick, D. W. CGRP ligand and receptor monoclonal antibodies for migraine prevention: evidence review and clinical implications. *Cephalalgia* **39**, 445-458 (2019).
42. Alexoudi, A., Donadio, V. & Karageorgiou, E. The potential role of CGRP in synuclein-associated neurodegenerative disorders. *Frontiers in Neuroscience* **18**, 1479830 (2024).
43. Singh, Y. *et al.* Calcitonin gene-related peptide (CGRP): A novel target for Alzheimer's disease. *CNS neuroscience & therapeutics* **23**, 457-461 (2017).
44. Na, H. *et al.* Characterization of the effects of calcitonin gene-related peptide receptor antagonist for Alzheimer's disease. *Neuropharmacology* **168**, 108017 (2020).
45. Zhang, J. & Zhong, Q. Histone deacetylase inhibitors and cell death. *Cellular and molecular life sciences* **71**, 3885-3901 (2014).
46. Bai, P. *et al.* HDAC11 displays neuropathological alterations and offers as a novel drug target for Alzheimer's disease. *Alzheimer's & Dementia* **21**, e14616 (2025).
47. Prakash, P. *et al.* Amyloid-β induces lipid droplet-mediated microglial dysfunction via the enzyme DGAT2 in Alzheimer's disease. *Immunity* **58**, 1536-1552. e1538 (2025).
48. Wang, Y. *et al.* TREM2 lipid sensing sustains the microglial response in an Alzheimer's disease model. *Cell* **160**, 1061-1071 (2015).
49. Xu, Z. *et al.* Microglia-specific regulation of lipid metabolism in Alzheimer's disease revealed by microglial depletion in 5xFAD Mice. *Nature communications* **16**, 9156 (2025).
50. Gao, M. *et al.* Loss of MFE-2 impairs microglial lipid homeostasis and drives neuroinflammation in Alzheimer's pathogenesis. *Nature Aging*, 1-18 (2025).
51. Kozlova, A. *et al.* PICALM Alzheimer's risk allele causes aberrant lipid droplets in microglia. *Nature* **646**, 1178-1186 (2025).
52. Haney, M. S. *et al.* APOE4/4 is linked to damaging lipid droplets in Alzheimer's disease microglia. *Nature* **628**, 154-161 (2024).
53. Cohen, H. *et al.* The neuropeptide Y (NPY)-ergic system is associated with behavioral resilience to stress exposure in an animal model of post-traumatic stress disorder. *Neuropsychopharmacology* **37**, 350-363 (2012).
54. Andersson, E. *et al.* Soluble cerebral Aβ protofibrils link Aβ plaque pathology to changes in CSF Aβ42/Aβ40 ratios, neurofilament light and tau in Alzheimer's disease model mice. *Nature Aging* **5**, 366-375 (2025).

Figures

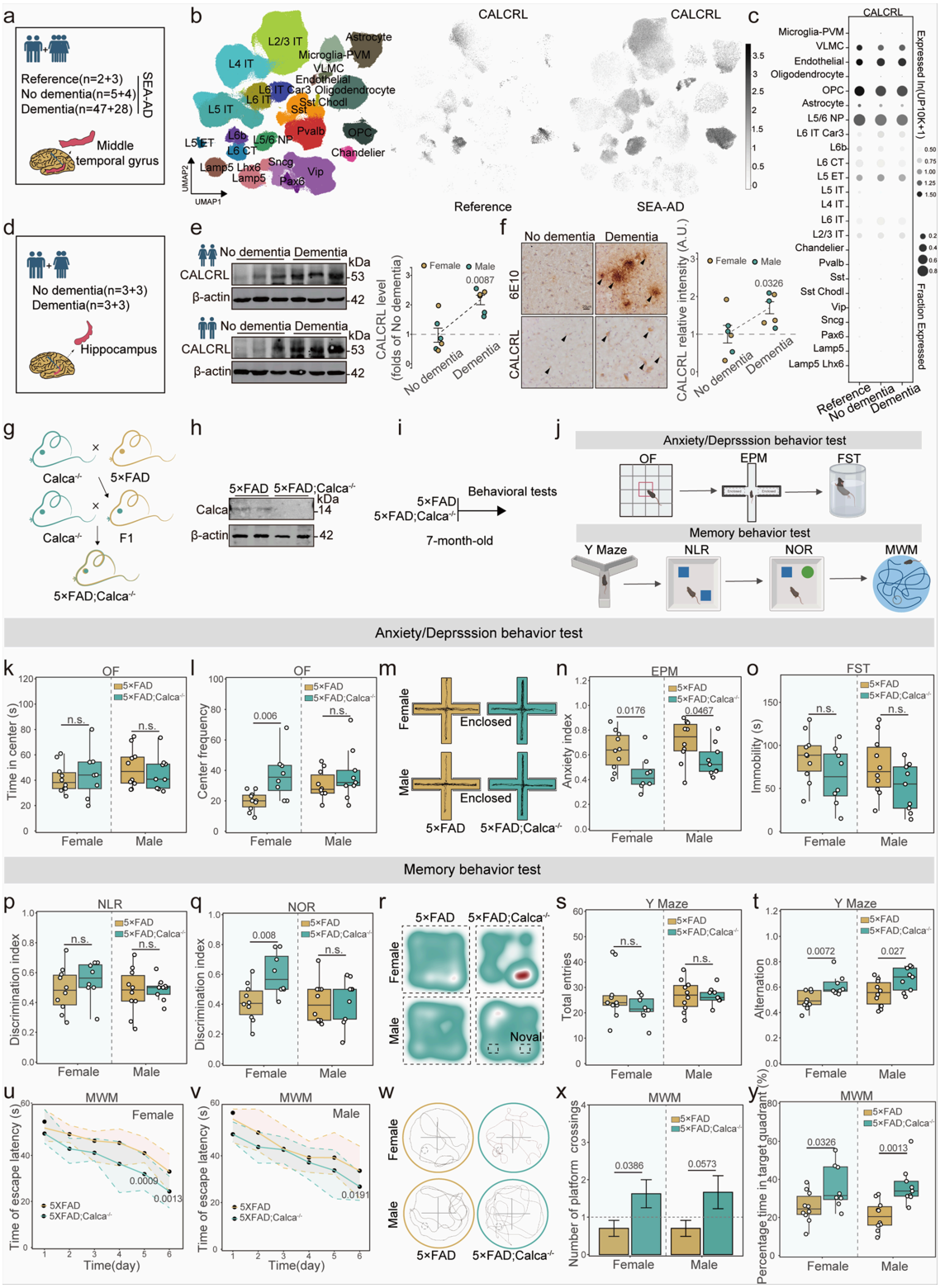


Figure 1

CALCRL is upregulated in patients with Alzheimer's dementia and 5×FAD mice, and *Calca* deficiency improves behavioral deficits in AD mice.

a, Characteristic information and the number of subjects in each group. **b**, UMAP of the associated cells expressing CALCRL in the reference and SEA-AD groups. **c**, CALCRL expression dot plot within each

sample. **d**, Characteristic information and the number of subjects in each group. **e**, Western blot image and densitometry analysis of CALCRL in human hippocampus. **f**, CALCRL and 6E10 immunohistochemistry and CALCRL semi-quantitative analysis in human hippocampus. Scale bars: 50 μm. **g**, Strategy for the generation of 5×FAD;Calca$^{-/-}$ mice. **h**, Western blot image analysis of α-CGRP proteins in the brain. **i**, Schematic representation of the experimental design. **J**, Cartoon schematic of the behavior experimental design. **k,l**, The results from the Open field test (OF). **m**, Representative movement traces of mice in the Elevated plus maze (EPM). **n**, The anxiety index calculated by the EPM. **o**, Immobility time in the Forced swim test (FST). **p**, The descrimination index (ratio of the number of explorations of the new location object to the total number of explorations) in the Novel location recognition (NLR) task. **q**, The descrimination index (ratio of the number of explorations of the new object to the total number of explorations) in the Novel object recognition (NOR) task. **r**, Representative movement heatmaps of the mice in the NOR task. s,t, The number of total arm entries (**s**) and spontaneous alternations (**t**) in the Y-maze test.

u-y, The results of Morris water maze (MWM). Latency to the platform in female (**u**) and male (**v**); Combined traces of the mice from each group during the probe test in the MWM (**w**); Entries into the platform zone (**x**); The percentage of time spent in target quadrant (**y**). Error bars indicate mean ± s.e.m. n.s., non-significant. Exact *n* and *P* values are presented in Supplementary Table 1. Image in **j** created in BioRender.

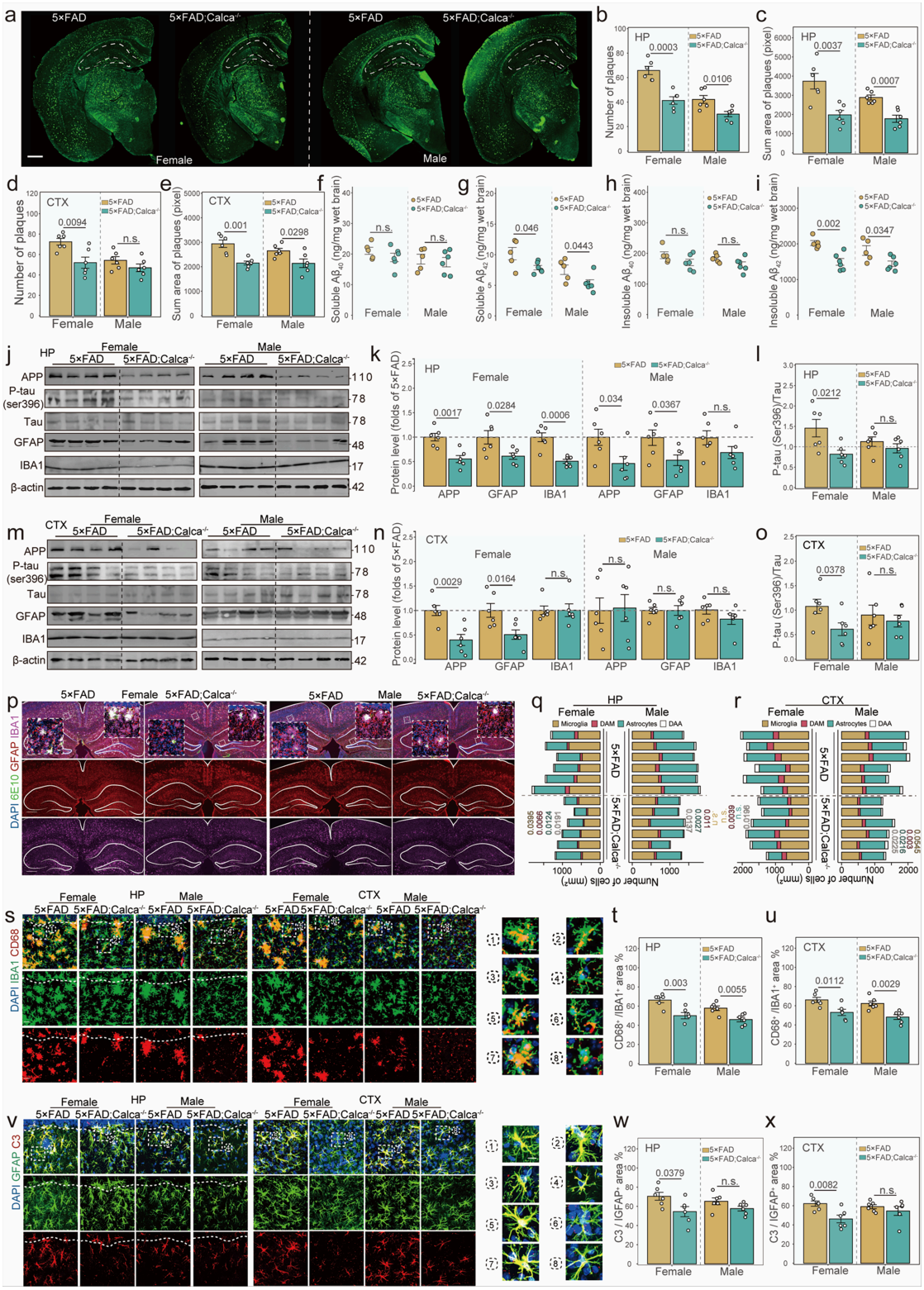


Figure 2

Calca deficiency ameliorates AD-related pathological features in 7-month-old 5×FAD mice.

a, Representative Thioflavin-S staining hippocampal images. Scale bar: 500 μm. **b,c**, Quantitative measurements of Aβ plaque numbers (**b**) and area (**c**) in the hippocampus. **d,e**Quantitative

measurements of Aβ plaque numbers (**d**) and area (**e**) in the cortex. **f-i**, ELISA quantification of soluble Aβ40 (**f**), soluble Aβ42 (**g**), insoluble Aβ40 (**h**), and insoluble Aβ42 (**i**) in the brains.

j-l, Western blot image (**j**) and densitometry analysis of APP, phosphorylated tau, total tau, GFAP and IBA1 in the hippocampus (**j,l**). m-o, Western blot image (**m**) and densitometry analysis of APP, phosphorylated tau, total tau, GFAP and IBA1 in the hippocampus (**n,o**). **p**, Immunofluorescence staining of 6E10 (green), GFAP (red) and IBA1 (pink). Scale bar:1 mm and 20 μm (ZOOM). **q,r**Quantification of total $GFAP^+$ astrocytes and $IBA1^+$ microglia, as well as Aβ-associated DAA (disease-associated astrocytes) and DAM (disease-associated microglia) in the hippocampus (**q**) and cortex (**r**). **s**, Immunofluorescence staining of IBA1 (green) and CD68 (red). Scale bar:20 μm and 10 μm (ZOOM). **t,u**, Quantification of $CD68^+/IBA1^+$ area fractions in the hippocampus (**t**) and cortex (**u**). **v**, Immunofluorescence staining of GFAP (green) and C3 (red). Scale bar:20 μm and 10 μm (ZOOM). **w,x**Quantification of $C3^+/GFAP^+$ area fractions in the hippocampus (**w**) and cortex (**z**). Error bars indicate mean ± s.e.m. n.s., non-significant. Exact *n* and *P* values are presented in Supplementary Table 1.

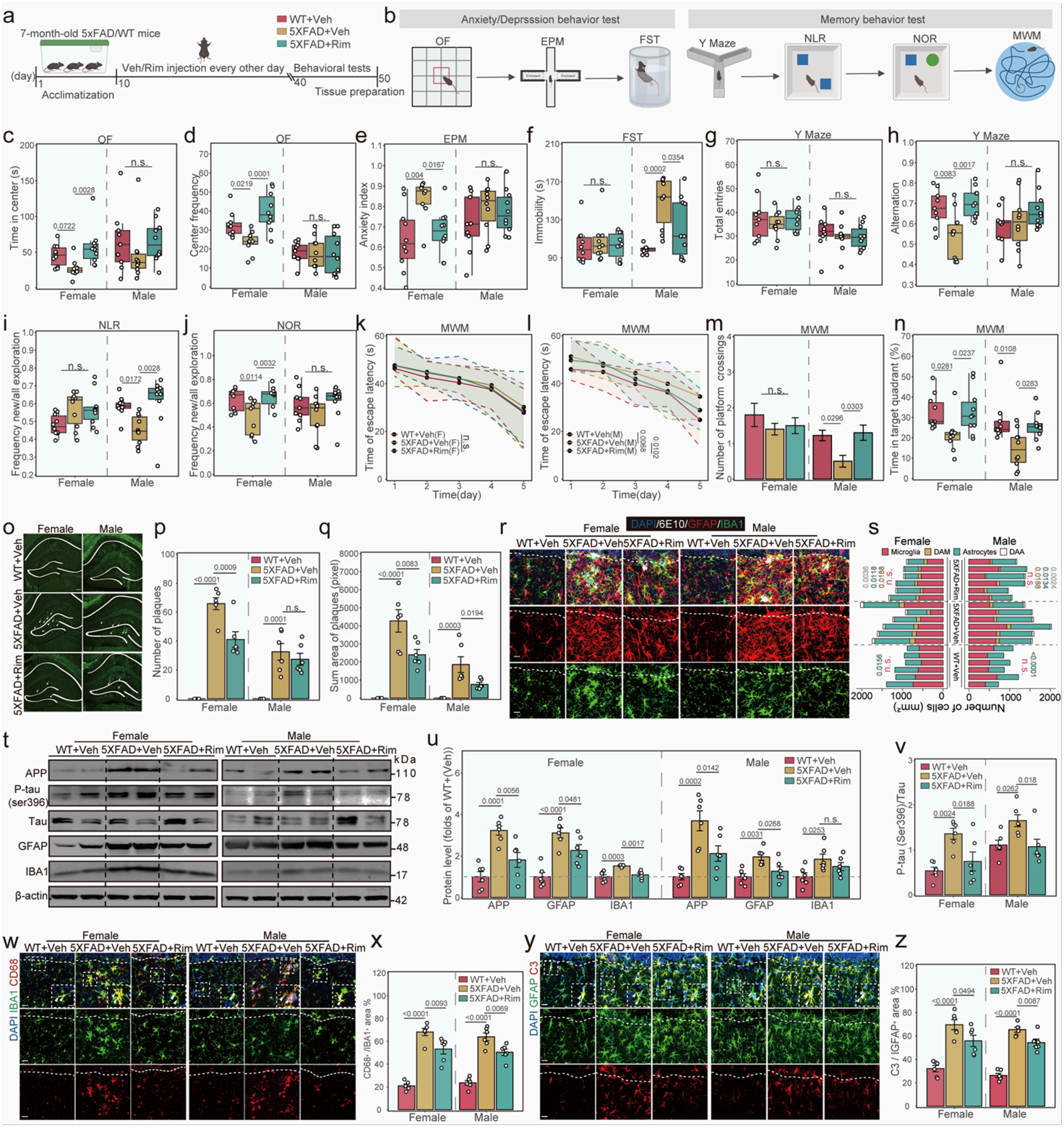


Figure 3

Rim alleviates behavioral deficits and AD-related pathological features in the hippocampus

a, Schematic representation of the experimental design. **b**, Cartoon schematic of the behavior experimental design. **c,d**, The results of the OF. **e**, The anxiety index of mice in the EPM. **f**, Immobility time of mice in the FST. **g,h**, The number of total arm entries and spontaneous alternations in the Y-maze

test. **i**, The descrimination index in the NLR task. **j**, The descrimination index in the NOR task. k-n, The results of Morris water maze (MWM). Latency to the platform in female (**k**) and male (**l**); Entries into the platform zone (**m**); The percentage of time spent in target quadrant (**n**). **o**, Representative Thioflavin-S staining hippocampal images. Scale bar: 100 μm. **p,q**, Quantitative measurements of Aβ plaque numbers (**p**) and area (**q**) in the hippocampus. **r**, Immunofluorescence staining of 6E10 (white), GFAP (red) and IBA1 (green) in the hippocampus. Scale bar: 20 μm and 10 μm (ZOOM). **s**, Quantification of total $GFAP^+$ astrocytes and $IBA1^+$ microglia, as well as Aβ-associated DAA (disease-associated astrocytes) and DAM (disease-associated microglia) in the hippocampus. **t-v**, Western blot image (**t**) and densitometry analysis of APP, BACE1, GFAP and IBA1 proteins (**u**), and the ratio of phosphorylated tau to total tau (**v**) in the hippocampus. **w**, Immunofluorescence staining of IBA1 (green) and CD68 (red) in the hippocampus. Scale bar: 20 μm and 10 μm (ZOOM). **x**, Quantification of $CD68^+/IBA1^+$ area fractions. **y**, Immunofluorescence staining of GFAP (green) and C3 (red) in the hippocampus. Scale bar: 20 μm and 10 μm (ZOOM). **z**, Quantification of $C3^+/GFAP^+$ area fractions. Error bars indicate mean ± s.e.m. n.s., non-significant. Exact *n* and *P* values are presented in Supplementary Table 1. Image in **a,b** created in BioRender.

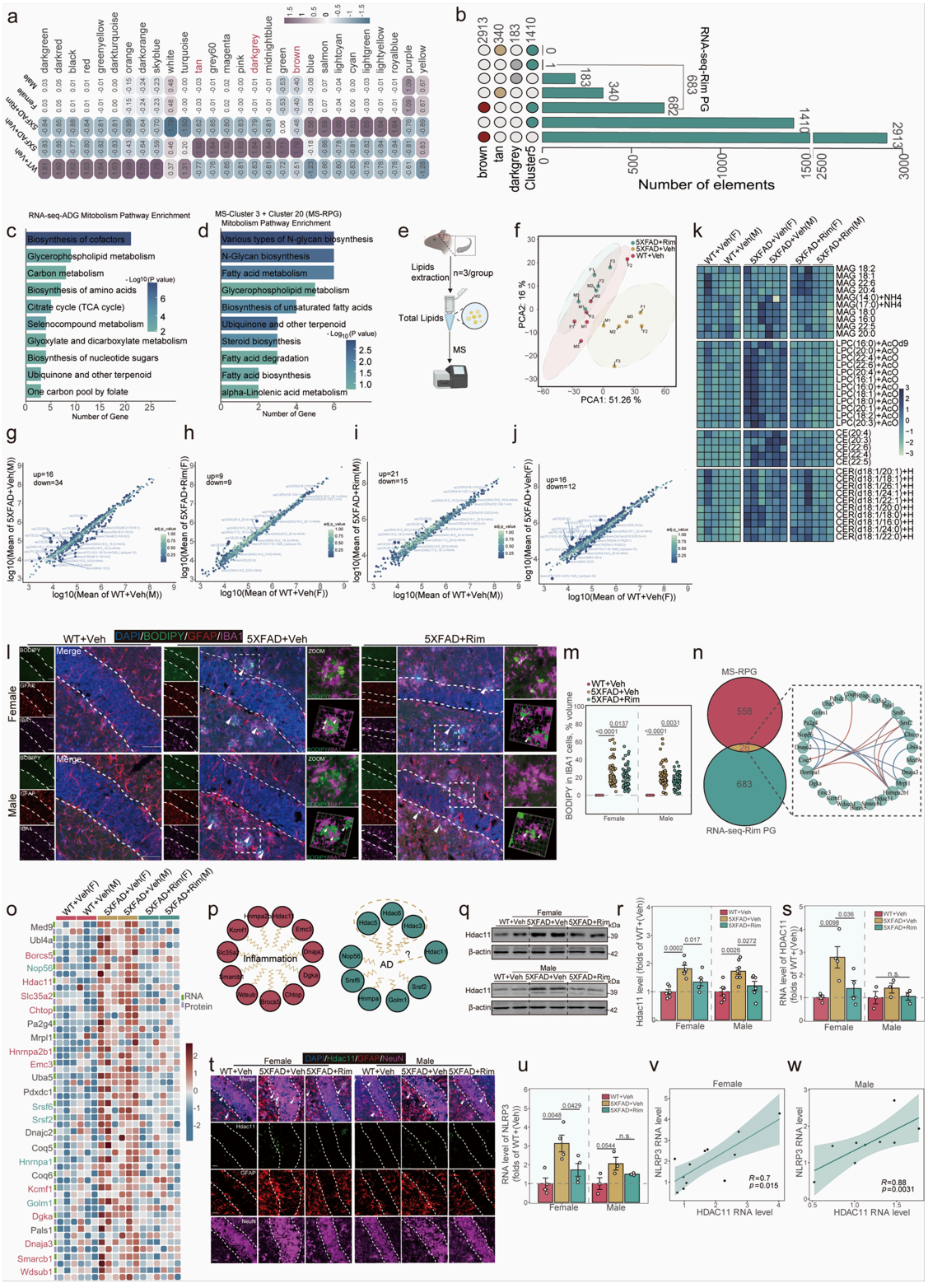


Figure 4

Rim reverses lipid metabolic changes, with HDAC11 closely associated with its efficacy in the hippocampus of 5×FAD mice

a, WGCNA module trait association correlation graph. **b**, WGCNA three AD-related modules and Mfuzz clustering analysis cluster 5 UpSet graph. **c**, KEGG metabolism pathways enrichment analysis of RNA-

seq-Rim PGs. **d**, KEGG metabolism pathways enrichment analysis of Cluster 3 and Cluster 20 (MS-RPG). **e**, Schematic representation of the experimental design. **f**, PCA based on results of lipidomic profiles obtained from MS. **g**, Volcano plot of differentially expressed lipids (DELs) in 5×FAD+Veh(F) vs. WT+Veh(F) mice. **h**, Volcano plot of DELs in 5×FAD+Veh(M) vs. WT+Veh(M) mice. **i**, Volcano plot of DELs in 5×FAD+Rim(F) vs. WT+Veh(F) mice. **j**, Volcano plot of DELs in 5×FAD+Rim(M) vs. WT+Veh(M) mice. **k**, Monoacylglycerol (MAG), lysophosphatidylcholine (LPC), cholesteryl ester (CE) and ceramide (CER) expression heat map.

l,m, Representative BODIPY (green), GFAP (red) and IBA1 (pink) co-staining with 3D-IMARIS rendering and quantification in the hippocampus. Scale bars: 50 μm and 10 μm (ZOOM). **n**, Venn diagram and protein-protein interaction (PPI) analysis of overlapping sets of RNA-seq-Rim PGs with MS-RPG. **o**, 26 overlapping genes expression heat map. p, Classification of inflammation-related genes and AD-related genes. **q,r**, Western blot image (**q**) and densitometry analysis of HDAC11 in the hippocampus (**r**). **s**, Quantitative PCR analysis of *Hdac11* RNA expression level in the hippocampus. **t**, Immunofluorescence staining of NeuN (Pink), GFAP (red) and Hdac11 (green)in the hippocampus. Scale bars: 20 μm. **u**, Quantitative PCR analysis of *Nlrp3* RNA expression level in the hippocampus. v,w, Correlation analysis of the RNA levels of *Hdac11* and *Nlrp3* in the hippocampus of female (**v**) and male mice (**w**). Error bars indicate mean ± s.e.m. n.s., non-significant. Exact *n* and *P* values are presented in Supplementary Table 1. Image in **e** created in BioRender.

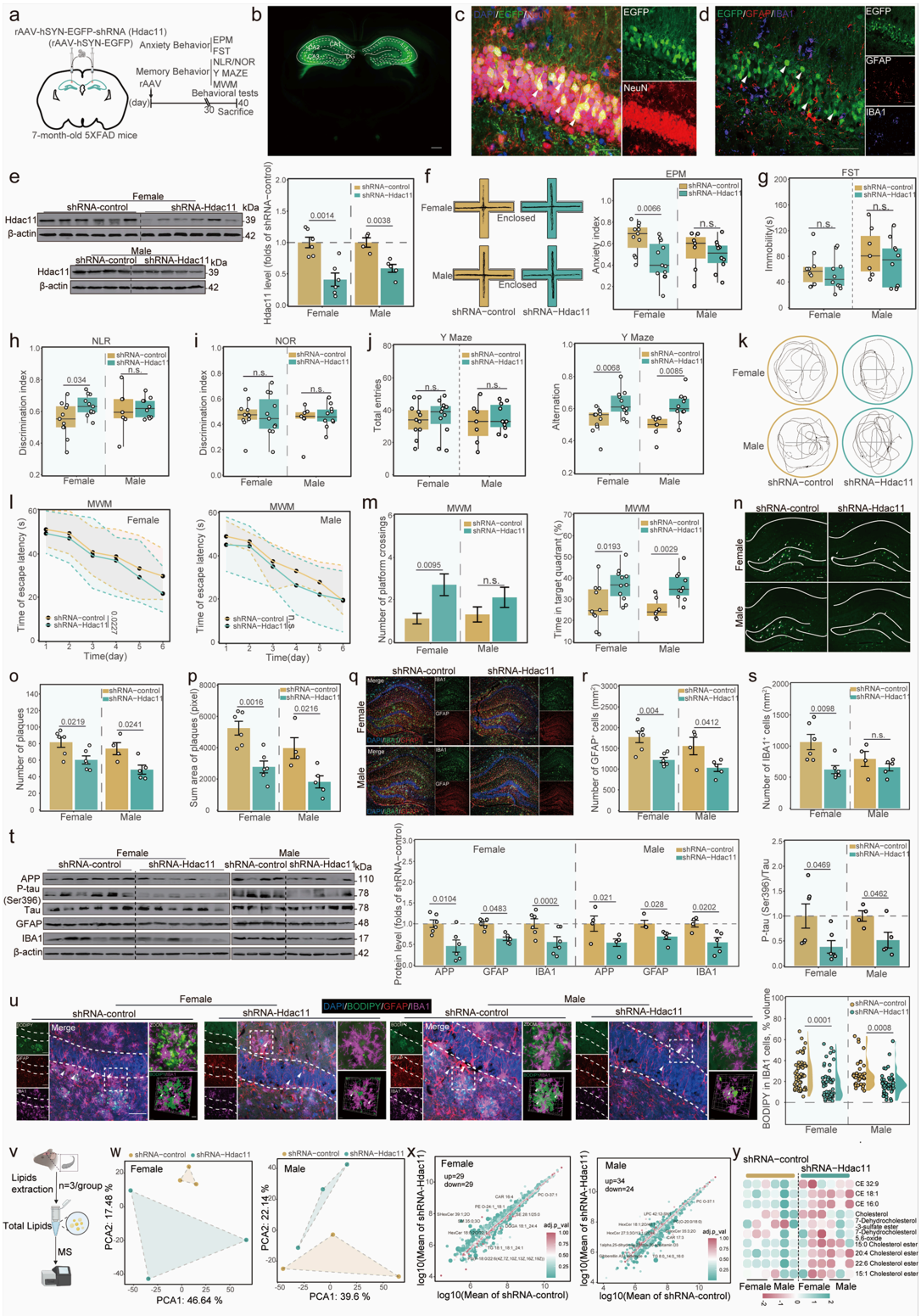


Figure 5

***Hdac11* knockdown in the hippocampus improves memory and alleviates pathology in 7-month-old 5×FAD mice.**

a, Schematic representation of the experimental design. **b**, Brain slices showing endogenous EGFP (viral infection). Scale bars: 1mm. **c**, Brain sections showing endogenous EGFP fluorescence (viral infection)

and NeuN immunostaining to label neurons. Scale bars: 50 μm. **d**, Brain slices were stained with EGFP (viral infection), GFAP (astrocyte) and IBA1 (microglia) antibodies. Scale bars: 50 μm. **e**, Western blot image and densitometry analysis of Hdac11 in the hippocampus. **f**, Representative movement traces of the mice in the EPM and the anxiety index. **g**, Immobility time in the Forced swim test (FST). **h**, The descrimination index in the NLR task. **i**, The descrimination index in the NOR task. **j**, The number of total arm entries and spontaneous alternations in the Y-maze test. k, Combined traces of the mice from each group during the probe test in the Morris water maze (MWM). **l,m**, The results of Morris water maze (MWM). Latency to the platform in female and male (**l**); Entries into the platform zone and the percentage of time spent in target quadrant in the MWM (**m**). n,Representative Thioflavin-S staining hippocampal images. Scale bars: 100 μm.

o,p, Quantitative measurements of Aβ plaque numbers (**o**) and area (**p**) in the hippocampus. **q**, Immunofluorescence staining of GFAP (red) and IBA1 (green in the hippocampus. Scale bars: 100 μm. **r,s**,Quantifications of $GFAP^+$ astrocytes (**r**) and $IBA1^+$ microglia (**s**) in the hippocampus. **t**, Western blot image and densitometry analysis of APP, phosphorylated tau, total tau, GFAP and IBA1in the hippocampus. **u**, Representative BODIPY (green), GFAP (red) and IBA1 (pink) co-staining with 3D-IMARIS rendering and quantification in the hippocampus. Scale bars: 50 μm and 10 μm (ZOOM). **v**, Schematic representation of the experimental design. w, PCA based on results of lipidomic profiles obtained from MS. **x**,Volcano plot of DELs in shRNA-Hdac11 vs. shRNA-control mice. **y**, Cholesterol metabolites expression heat map. Error bars indicate mean ± s.e.m. n.s., non-significant. Exact *n* and *P* values are presented in Supplementary Table 1.

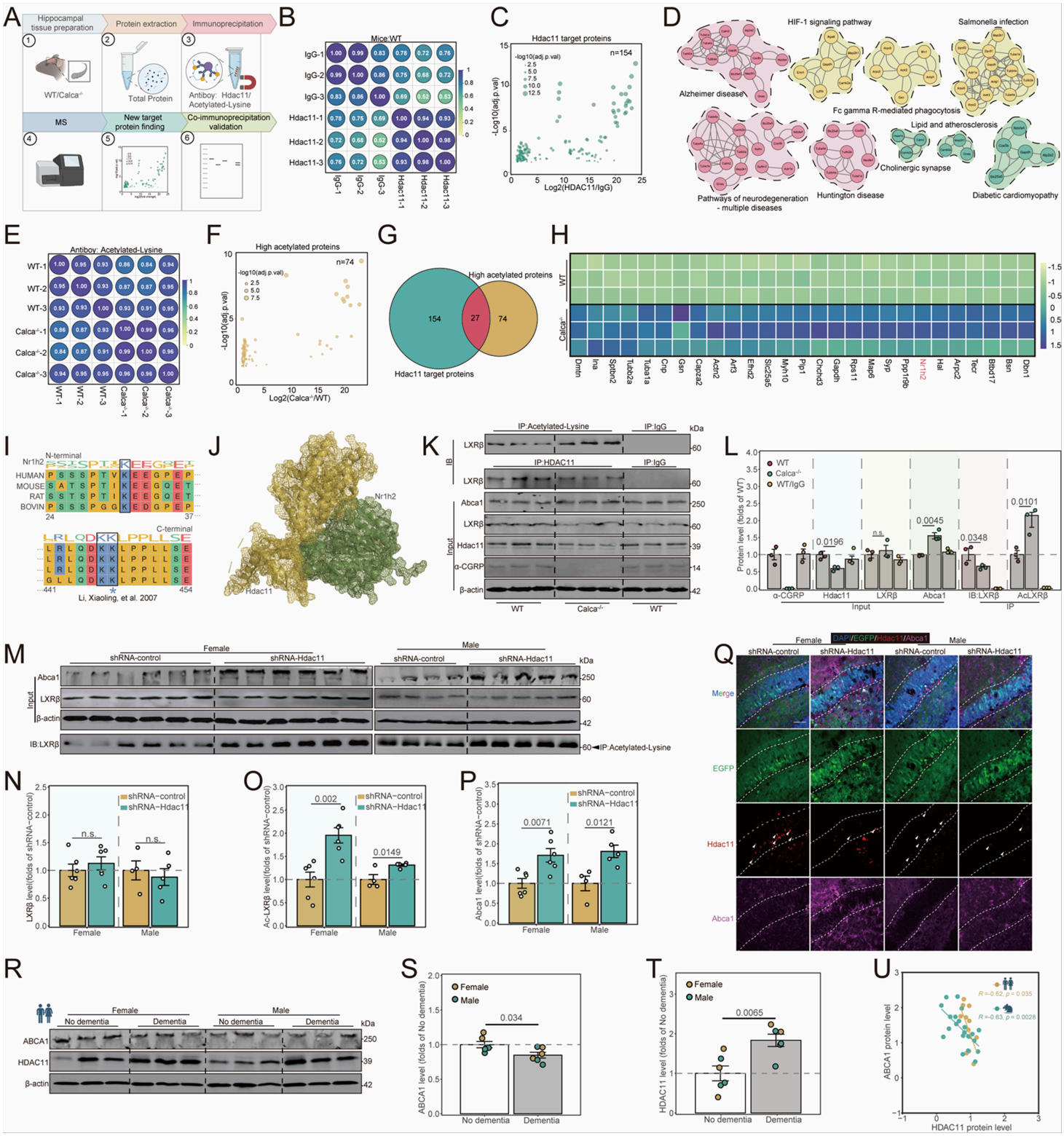


Figure 6

Knockdown of *Hdac11* exerts a protective role *in vivo* by targeting LXRβ/ABCA1 axis.

a, Schematic representation of the experimental design. **b**, Correlation analysis of IgG and Hdac11 antibody groups. **c**, Scatter plot depicting the 154 Hdac11-interacting candidates from the immunoprecipitation/mass spectrometry (IP-MS). **d**, Protein-protein interaction (PPI) network analysis of

the Hdac11 target proteins that belong to the enriched KEGG pathways. **e**, Correlation analysis of WT and *Calca*$^{-/-}$ groups. **f**, Scatter plot depicting the 74 highly acetylated proteins from the IP-MS. **g**, Venn diagram of overlapping sets of Hdac11 target proteins with highly acetylate proteins. **h**, 27 overlapping proteins expression heat map. **i**, Protein sequence alignment of NR1H2/LXRβ across species. **j**, Protein–protein docking and molecular dynamics of Hdac11 (yellow) bound to NR1H2 (green). **k,l**, Hippocampal protein lysates from WT or *Calca*$^{-/-}$ mice were precipitated with Hdac11, acetylated-lysine, or IgG antibodies and then analyzed by Western blotting (**k**), followed by statistical analysis (**l**). **m-p**, Hippocampal protein lysates from shRNA-control or shRNA-Hdac11 administrated 5×FAD mice were precipitated with acetylated-lysine antibodies and then analyzed by Western blotting (**m**) followed by statistical analysis (**n-p**). q, Brain slices were stained with EGFP (green), Hdac11 (red), and Abca1 (pink) antibodies. Scale bars: 50 μm. **r-t**, Western blot image (**r**) and densitometry analysis of HDAC11 (**s**) and ABCA1 (**t**) in human hippocampus. **u**, Correlation analysis of the protein levels of HDAC11 and ABCA1. Error bars indicate mean ± s.e.m. n.s., non-significant. Exact *n* and *P* values are presented in Supplementary Table 1. Image in **a** created in BioRender.

Supplementary Files

This is a list of supplementary files associated with this preprint. Click to download.

- ExtendedDataFig.5.tif
- SupplementaryTable2.xlsx
- SupplementaryTable3.xlsx
- SupplementaryTable1.xlsx
- ExtendedDataFig.1.tif
- ExtendedDataFig.4.tif
- ExtendedDataFig.8.tif
- ExtendedDataFig.9.tif
- ExtendedDataFig.7.tif
- ExtendedDataFig.6.tif
- ExtendedDataFig.10.tif
- ExtendedDataFig.2.tif
- ExtendedDataFig.3.tif
- Extendeddata.docx